Sputtered Silicon Oxynitride for Microphotonics: A Materials Study

by

Jessica Gene Sandland

S.B. Materials Science and Engineering
Massachusetts Institute of Technology, 1999

Submitted to the Department of Materials Science and Engineering in Partial Fulfillment of the Requirements for the Degree of

Doctor of Philosophy in Electronic Materials
at the
Massachusetts Institute of Technology

February 2005

Signature of Author: _____

Department of Materials Science and Engineering
October 28th, 2004.

Certified by: _____

Lionel C. Kimerling
Thomas Lord Professor of Materials Science and Engineering
Thesis Supervisor

Accepted by: _____

Carl V. Thompson II
Stavros Salapatas Professor of Materials Science and Engineering
Chair, Departmental Committee on Graduate Students

Sputtered Silicon Oxynitride for Microphotonics:

A Materials Study

by

Jessica Gene Sandland

Submitted to the Department of Materials Science and Engineering on October 28,2004, in Partial Fulfillment of the Requirements for the Degree of Doctor of Philosophy in Electronic Materials

ABSTRACT

Silicon oxynitride (SiON) is an ideal waveguide material because the SiON materials system provides substantial flexibility in composition and refractive index. SiON can be varied in index from that of silicon dioxide (n=1.46) to that of silicon-rich silicon nitride (n~2.3). This flexibility in refractive index allows for the optimization of device performance by allowing trade-offs between the advantages of low-index contrast systems (low scattering losses and easy fiber-to-waveguide coupling) and the benefits of high-index-contrast systems (small waveguide size and tight bending radii).

This work presents sputter processing as an alternative to traditional CVD processing. Two room-temperature SiON sputter processes are explored. The first process is a co-sputtered deposition from a silicon oxide and a silicon nitride target. The second is a reactive sputtering process from a silicon nitride target in an oxygen ambient. Silicon nitride sputtered from a silicon nitride target is also investigated.

Models are provided that predict the index and composition in both the reactive and co-sputtered depositions. The cosputtered deposition is shown to follow a mixture model, while the reactive sputter deposition is shown to be either Si-flux limited or O-flux limited, depending on the partial pressure of oxygen in the reaction chamber and the power applied to the silicon nitride target. A materials study is provided that shows sputtered SiON to be a homogeneous material that gives good control of refractive index. Reactively sputtered SiON is shown to be Si-rich.

These sputtered materials investigated for use in waveguides and in Er-doped waveguide amplifiers. Low loss waveguides are demonstrated for both co-sputtered and reactively sputtered depositions. Losses below 1 dB/cm are shown for co-sputtered deposition (n=1.65). Photoluminescence of Er-doped material shows lifetimes comparable to commercial EDFA material for both co-sputtered SiON and sputtered silicon dioxide.

Silicon dangling bonds are shown to contribute both to the losses in the waveguides and to the non-radiative energy transfer in the Er-doped material.

Thesis Supervisor: Lionel C. Kimerling

Title: Thomas Lord Professor of Materials Science and Engineering

Acknowledgments

There are many people who made this work possible. Some provided scientific support, others provided emotional support, and I am grateful to every one.

My advisor, Prof. Lionel Kimerling, provided the support and feedback that allowed me to grow as a scientist during my many years in the EMAT group. He also provides the example that makes EMAT such a great place to work. Kim, it has truly been a privilege to work with you.

Anat Eshed is a great scientist and a great friend, and her insights into this work have been invaluable. She also kept the sputtering machine alive, and taught me more than I ever though I'd know about vacuum systems. Thanks Anat!

To my collaborators, I thank you. This work wouldn't be complete without Sajan Saini's contributions on erbium luminescence and Shoji Akiyama's channel waveguide measurements. I'd also like to thank Xiaoman Duan for her TEM micrographs.

EMAT has been a wonderful place to work and study, thanks to all of the friendly and creative folks in the group. Mindy Baughman keeps everything in EMAT running smoothly; her efforts make our science possible. Jurgen Michel and Anu Agarwal always have their doors open for quick questions and important discussions. Douglas, Yasha, Dan, Shoji, Victor, Donghwan, Nok, Dave, Trisha, Luca, Jifeng, Jae Hyung, Ching-Yin, and Mike -- thank you for being great lab mates, I've learned so much from each of you.

I'd like to thank Prof. Caroline Ross for the use of her group's RGA, without which I would not have been able to complete this work.

Finally, I'd like to thank my friends and family. Mom and Dad, thanks for all of your love and support through many, many years of MIT. Kyle, thank you for carting my husband back and forth to work so that I could get to campus every day. I'd like to give a

special thanks to Mark for having the good sense to move to California right before I started writing my thesis, so that I'd have someone to talk to at two in the morning.

Finally, I'd like to give a special thanks to my husband, Ruben, for his love, support and good humor throughout this entire experience.

Contents

List of Figures

List of Tables

Chapter 1

Introduction

1.1 Background

The past fifty years have seen a communications revolution that has transformed the way people think about, store, and transmit information. Developments in microelectronics have put a personal computer on every desktop. This ubiquitous computer has dramatically increased our ability to store and process information. Likewise, evolutions in telecommunications allow for the transfer of information at unprecedented rates. The development and implementation of ultra-low-loss optical fibers, in conjunction with their associated lasers, amplifiers, and detectors, has produced an unparalleled means of transferring and communicating information [1].

As the ability to rapidly process and transmit information has grown, our reliance on the ability to quickly transfer data has also increased. The demands placed on computer proces-

sors and information networks continue to grow. The Semiconductor Industry Association predicts that by 2010, local clock speeds will exceed 15 GHz [2]. In order to accommodate these ever-increasing demands on processors and networks, new technologies must evolve that can provide the desired speeds.

Microphotonics has the ability to provide the computing and data transfer speeds that will soon be required. Microphotonics is the optical equivalent to microelectronics, where light is communicated and manipulated at the micron scale. Microphotonics has the potential to increase communications speeds at all levels, from wide area networks to processor clock speeds.

The realization of microphotonic communication will require the development and optimization of a variety of micro-optical devices. A basic optical link requires a light emitter (laser) to emit light, a waveguide to transfer the light, and a detector to detect the incoming signal [3]. In addition to these basic components, a variety of other supporting devices must be developed, including amplifiers, modulators, splitters, and filters. The work in this thesis focuses on materials for waveguide and other light transfer applications.

The choice of materials system is critical to the design and performance of an optoelectronic system. III-V semiconductors are sometimes preferred because all photonic components, including lasers, can be produced with III-V systems; additionally, the high mobility of III-V systems produces fast devices [4]. Silicon and silicon-compatible systems provide

an alternative to III-V microphotonics. Silicon based systems have a number of benefits. Silicon technology is very well established; therefore, there is a large body of processing knowledge that can be drawn upon. Silicon is also inexpensive, and it can be fully integrated with CMOS processing. Because of these benefits, this work will focus on silicon-based technologies. The largest hurdle in employing a silicon microphotonics system is that the indirect bandgap of the group-IV semiconductors prevents the production of a silicon-based laser. This limitation, however, is easily overcome by moving the light emitter off-chip while fully integrating the remainder of the microphotonic devices. Once this limitation is addressed, the well-developed, inexpensive silicon system becomes the ideal platform for microphotonics.

Another critical design choice is the index contrast for the waveguide devices. The index contrast of the system, which is defined as $(n_{core} - n_{cladding})/n_{core}$, determines a variety of things about the waveguide performance [5]. First and foremost, the index contrast of the system determines how well light is confined within the waveguide. A high-index-contrast system confines the light very well to the waveguide core, and the mode size is small. Because of this small mode size, the waveguide dimensions can also be small. High-index-contrast silicon waveguides can be made with device dimensions well under a μm^2 [6]. Conversely, the light is a low index contrast waveguide is poorly confined to the core, and the mode size is quite large. This large mode requires that the waveguide dimensions be quite large. Low-index-contrast silica wave guide can be several μm on a side [7] [8].

The choice of index contrast also has consequences in waveguide performance. Losses due

to surface scattering are much higher in high-index-contrast systems. Because of both mode mismatch (caused by coupling from a low index fiber to a high index waveguide) and alignment difficulties (because the device sizes are small), coupling losses are also higher in high-index-contrast systems. On the other hand, high index contrast systems give a dramatic benefit whenever the waveguide needs to bend. The bending radii of high-index-contrast systems can be on the order of a micron [9]. The bending radii of low-index-contrast systems can approach 1cm [10]. This fundamental limitation to the miniaturization of very-low-index-contrast bends means that these systems can only be employed in cases where a large device footprint is not an issue.

Because there are so many tradeoffs when choosing a refractive index, it is important that device designers have the flexibility to specify index contrast. The silicon oxynitride (SiON) materials system has the potential to allow device designers to choose from a very wide range of index contrasts. Silicon oxynitride can be varied in index and composition from that of SiO_2 (n=1.46) to that of silicon-rich Si_3N_4 (n= about 2.3, depending of the silicon content of the nitride). The wide range of indices achievable with SiON allows for the selection and variation of a variety of indices while still remaining in the SiON materials system.

1.2 Overview

Current silicon oxynitride processing technologies do not fully exploit the potential of the SiON system. Hydrogen incorporation, high film stresses, high absorption at 1550 nm, and the need for high- temperature anneals restrict current SiON processing. These processing difficulties make it hard to achieve a full range of refractive indices and create a CMOS compatible process. The goal of this thesis is to study sputter processing as an alternative to traditional SiON technologies. The aim of this work is to develop a SiON sputter deposition process that is well-understood, easily tuned, CMOS compatible and easily tailored to allow for doping and other materials modifications.

Chapter two provides an overview of traditional SiON processing technology. The advantages and disadvantages of PECVD and LPCVD processing are discussed. Sputter deposition is presented as an alternative processing method, and some basic background to sputter deposition is presented. Chapter three gives an analysis of the quality of sputtered silicon oxynitride materials. Materials which have been prepared under a variety of processing conditions are analyzed. The compositional and structural properties of these films are considered. The properties of these materials are evaluated in order to ensure good materials quality and to gain a full understanding of this sputter process. Chapter four utilizes residual gas analysis to understand the products and bi-products of the sputter deposition process. Chemical reactions are given for a variety of sputter processes, and a model is presented to predict the quality and composition of the sputtered materials. Chapter five investigates the optical properties of silicon nitride and silicon oxynitride

waveguides. Slab waveguide loss measurements are given for materials processed under a variety of conditions, and these losses are correlated to the chemical and morphological properties presented in earlier chapters. Channel waveguide measurements for silicon nitride waveguides are also presented. Chapter six gives an evaluation of sputtered silicon oxynitride as a host to erbium atoms for light amplification. SiON photoluminescence is considered in the context of the deposition conditions and materials properties. Chapter seven gives the conclusions to this work and provides an outline for future work.

Chapter 2

Silicon Oxynitride Processing: An Overview

2.1 Silicon-Based Materials Systems for Waveguiding

Over the past decade, much optical communications research has focused on planar waveguide structures for application in both optical sensors and interconnects [15]. Devices used for integrated optics must meet a number of requirements. These devices must exhibit low losses and efficient fiber-to-chip coupling [16]. Additionally, these structures should show polarization-independent behavior, and they should allow for small bending radii so that a high integration density can be realized [17]. First-generation planar lightwave circuits (PLCs) employing silica-based devices are now commercially available, and much research is going into improving these technologies to produce the next generation of integrated optical devices [18].

2.1.1 Silica Technology

Conventional PLC waveguides consist of three layers of silica deposited on a silicon substrate. The optically guiding core consists of silica that has been doped with germanium, phosphorus, or titanium in order to raise the refractive index of the silica. Typical index contrasts of silica waveguides are between 0.005 and 0.007 [18]. These very low index contrasts limit surface scattering, and silica channel waveguides with propagation losses below 0.1 dB/cm have been realized [15]. Additionally, the index contrast of these silica waveguides is approximately the same as the contrast of silica optical fibers. Therefore, the single mode waveguide dimension of silica waveguides is similar to that of optical fibers, allowing for efficient fiber-to-waveguide coupling. Coupling losses of around 0.1 dB per facet have been demonstrated in silica systems [18].

Silica planar lightwave circuits posses major limitations, however. The minimum achievable radius of curvature for these low index contrast waveguides is quite large; bending radii of 15-20 mm are typical [15]. These waveguide dimensions significantly limit the integration densities achievable with silica optical devices. With complicated structures such as arrayed waveguide gratings, such low integration densities and large chip dimensions become prohibitive [18]. Furthermore, the dopants traditionally employed to raise the index contrast of silica waveguides offer a very limited range of potential refractive indices. Figure 2.1 shows the range of refractive indices achievable through boron, phosphorus and germanium doping. This figure demonstrates that it is impossible to achieve higher index contrasts using these traditional dopants. Furthermore, the large mode size of low-index-contrast

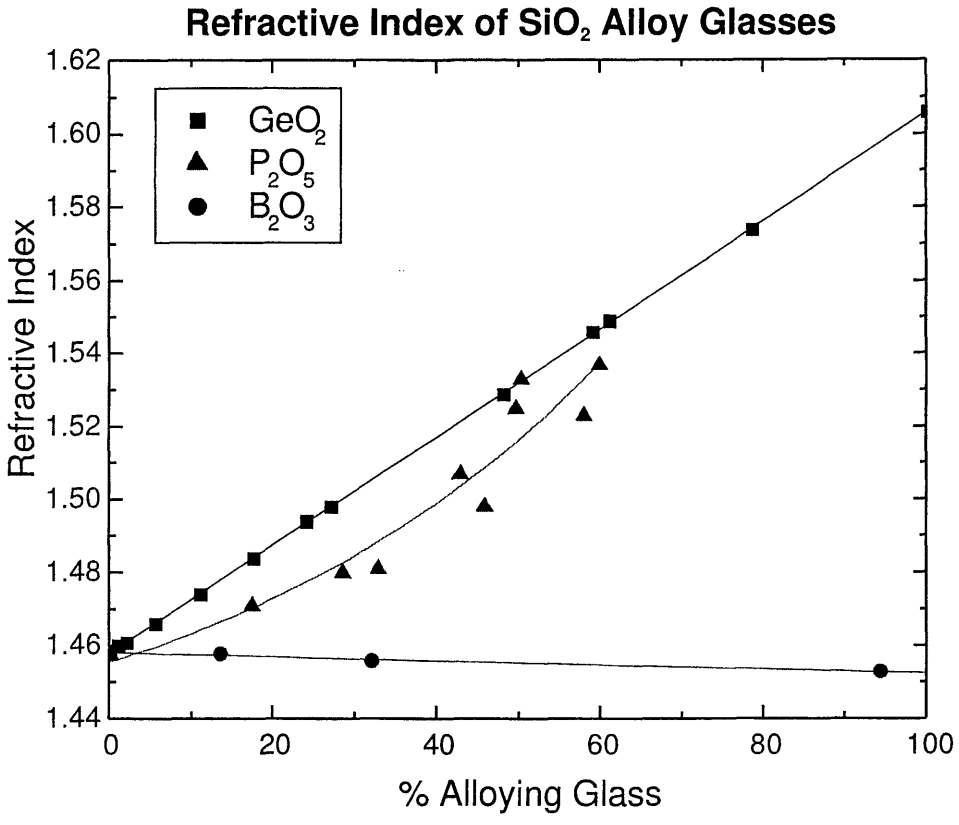

Figure 2.1: Refractive indices of various bulk silica alloys [97]

silica waveguides often require the use of specialized thick film deposition techniques, such as flame hydrolysis deposition [104]. Flame hydrolysis deposition requires the use of high temperatures that are not compatible with CMOS processing.

2.1.2 High Index Contrast Waveguides

High index contrast (HIC) silicon and silicon nitride waveguides have emerged as an alternative to the large footprint silica waveguides described above. These waveguides utilize a high index core material surrounded by a low index silica cladding. The index difference in these HIC waveguides ranges from about 0.56 (for silicon nitride, depending on the nitride's stoiecheometry) to 2.0 (for silicon). These very high index contrasts allow for the creation of very compact devices with very small bending radii. Lee et al. report a bending loss of less than 3dB for a bending radius of 3 μm, and they have fabricated a 1x16 optical power splitter in an area smaller than 0.0001 cm^2 [20]. However, surface scattering from these waveguides can be significant, and fiber-to-waveguide coupling can be very difficult due to the large mode size mismatch between the fiber mode and the waveguide mode, leading to high insertion losses.

2.1.3 The Promise of Silicon Oxynitride

Silicon oxynitride (SiON) waveguide technology is emerging as potential alternative to silica technology. The index of SiON can be tuned continuously between that of silica (1.45) and that of silicon nitride (2.0) [16]. This wide range of potential refractive indexes has a number of advantages. First, the device designer can select among a wide range of refractive indices, increasing the flexibility of device design. Higher index contrasts can be chosen to decrease bending radii and increase device integration densities. Lower index contrasts can be used to achieve high efficiency fiber-to-chip coupling. Additionally, most techniques used in SiON processing are well-developed and compatible with standard

silicon integrated circuit process technology [17]. This compatibility makes possible a CMOS compatible SiON integrated optics technology.

Unfortunately, there are still a number of difficulties with SiON waveguide technology. Plasma enhanced chemical vapor deposition (PECVD), the fastest and most economical method of SiON processing currently employed, results in a large amount of hydrogen incorporation in films. This hydrogen dramatically increases absorption in the 1550 nm wavelength range [18]. Very high temperature anneals (>1100 C) can be used to decrease, but not eliminate, excess hydrogen incorporation. However, such anneals lead to high film stresses, and they eliminate the possibility of designing a CMOS compatible SiON technology. Furthermore, this hydrogen incorporation restricts the range of achievable SiON indexes.

In this work, sputter processing is investigated as an alternative to traditional CVD SiON deposition. Sputter processing has been used for decades to deposit dielectric coatings and metallic microelectronic interconnects. Sputtering provides a flexible and relatively quick method for depositing alloys whose compositions need to be tuned in order to provide for specific materials properties.

2.2 Current Silicon Oxynitride Processing Technology

2.2.1 PECVD SiON Processing Technology

Plasma enhanced chemical vapor deposition has emerged as the preferable method of silicon oxynitride deposition. Though exact SiON waveguide processing parameters vary from laboratory to laboratory, the next section provides an overview of a typical SiON waveguide process.

Silicon Oxynitride Processing

Germann et al. report a typical SiON waveguide processing scheme [18]. First, a lower cladding layer is grown by thermal oxidation of the silicon substrate. A SiON waveguide layer is then deposited by PECVD. The gaseous precursors used are silane (SiH_4) diluted in 2% helium, nitrous oxide (N_2O) and ammonia (NH_3). The relative gas flow rates of the three gasses can be adjusted to vary the refractive index of the guiding layer. The substrate is maintained at 400°C during deposition. An 1140°C anneal in nitrogen is used to densify the SiON and drive off excess hydrogen introduced by the gas precursors. The core is patterned using reactive ion etching, and a PECVD SiO_2 upper cladding is deposited. A schematic of a typical 3-layer SiON channel waveguide is shown in Figure 2.2.

Figure 2.3 shows the variation of refractive index with increasing nitrous oxide/silane flow ratio. This figure demonstrates that an entire range of indices from SiO_2 to Si_3N_4 can be

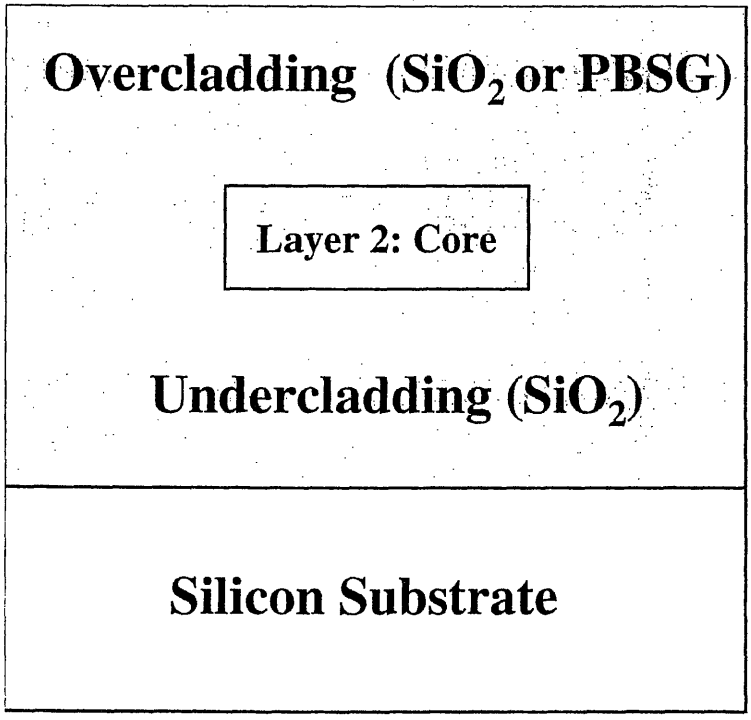

Figure 2.2: Typical channel waveguide layout. The core layer can be made from a number of materials, including SiON, Si, Si_3N_4, and doped-SiO_2. The dimensions of the waveguide will depend on the index contrast of the system.

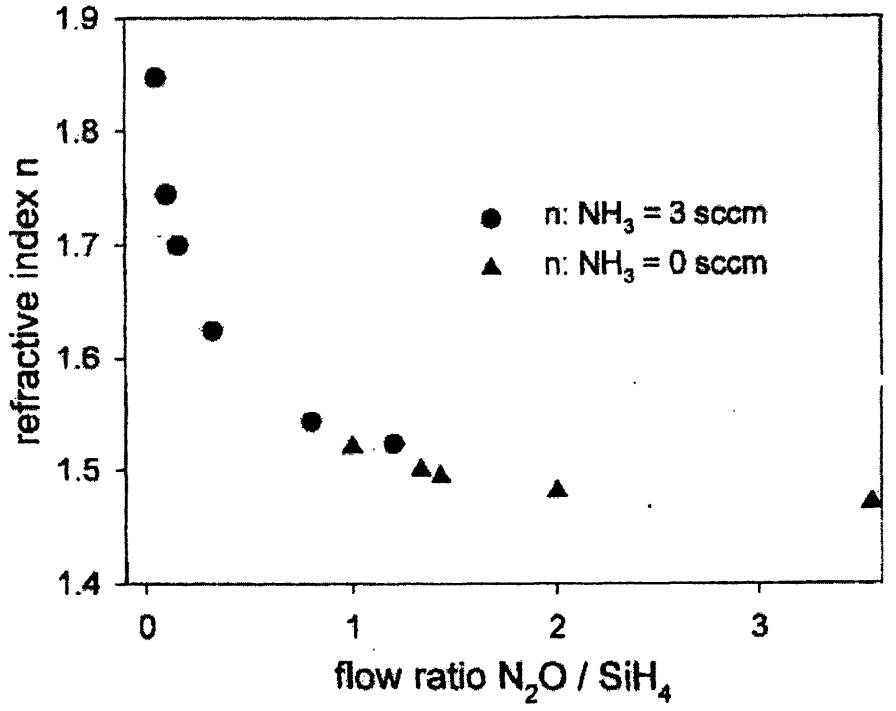

Figure 2.3: Refractive index vs. gas flow rate of PECVD process where P=60 W, p=650 mtorr, T = 300°C. From de Ridder et al. [17]

obtained with PECVD silicon oxynitride. Figure 2.3 also illustrates a significant drawback to PECVD SiON technology. Integrated optical technologies require very accurate adjusting of the index of refraction. Unfortunately, at indices above about 1.7, a small change in gas flow rate produces a very large change in refractive index, making it difficult to achieve the required index accuracy [16].

Hydrogen Incorporation in PECVD Silicon Oxynitride Films

Hydrogen incorporation into the SiON film provides the primary obstacle to the creation of a viable PECVD silicon oxynitride integrated optical technology. Hydrogen incorporation in these films occurs in the form of N-H, O-H, and Si-H bonds, or as excess hydrogen [22, 24]. The N-H and Si-H absorption peaks are clearly visible. Nitrogen-hydrogen bonds are the primary cause of waveguide loss in the optical operating window of 1540-1560 nm [23]. The first overtone of the N-H vibrational bond occurring at 3382 cm^{-1} produces an absorption peak centered on 1510 nm. [22].

Worhoff et al. provide a thorough study of the influence of annealing conditions on losses in SiON waveguides [21]. The optical losses in slab PECVD SiON waveguides at 1550 nm wavelength was measured to be 1.8 dB/cm at lower refractive index (n=1.48) and 10 dB/cm at higher refractive index (n=1.68). Annealing for 1 hour in air at 1150°C reduced the low index waveguide loss to 0.2 dB/cm at 1550 nm wavelength.

On a final note, Sanchez et al. PECVD deposited silicon oxynitride films using $SiCl_4$ for use in microelectronic devices [26]. Sanchez et al. deposited SiON films using $SiCl_4$, O_2, and NH_3 at 250°C in order to decrease the amount of hydrogen in the films, thus decreasing the required time and temperature of the anneal. Though these deposition conditions produced a successful reduction in the amount of hydrogen in the films, these conditions produced films two orders of magnitude more rough than those produced with a standard PECVD process.

Other Considerations

Worhoff et al. report good uniformity and run-to-run reproducibility for PECVD silicon oxynitride with n<1.55 [21]. The refractive index inhomogeneity was shown to be 2-6 x 10^{-4}, and the thickness non-uniformity was 0.8% over a 50x50mm area. The run-to-run refractive index inhomogeneity was 6 x 10^{-4}, and the thickness non-uniformity was measured at 1%. Germann et al. have reported waveguide birefringences below 1 x 10^{-4} by optimizing the deposition and annealing steps and by etching stress release trenches next to the waveguide core [18].

Deuterium

Replacing the hydrogen in PECVD deposited silicon oxynitride films with deuterium has been proposed as a method to reduce or eliminate the absorption associated with N-H bonding. The higher mass of deuterium shifts the bond resonance away from the critical 1550nm wavelength window. The substitution of deuterium for hydrogen can be accomplished in one of two manners. Lee et al. deposit silicon oxynitride using a standard PECVD process, and then annealed these films in a deuterium ambient [64]. Alternatively, Shih et al. elects to substitute the hydrogen-containing precursors (SiH_4 and NH_3) with deuterium-containing precursors (SiD_4 and ND_3) [65]. The use of deuterium as a substitute for hydrogen in PECVD SiON films shows promise. Lee et al. have demonstrated waveguide losses as low as 0.48 dB/cm using their isotope exchange method (after an anneal at 950°C in a deuterium ambient). They contrast this with the 1.0 dB/cm losses achievable using their traditional processing technique (after an anneal at 1145°C).

2.2.2 Current LPCVD Technology

Since high-quality, high refractive index thin films cannot be deposited using PECVD, low pressure chemical vapor deposition (LPCVD) has emerged as the preferred method for depositing high index (n<1.7) silicon oxynitride waveguides [27] [100]. Worhoff et al. use SiH_2Cl_2, O_2 and NH_3 as the precursors in a reactor kept at a temperature of 800-900°C and a pressure of 50 to 200 mtorr to deposit films with indices ranging from 1.7 to 2.0 [27]. Deposition rates as low as 3 nm/min, along with the high deposition temperatures required, provide the primary obstacles to LPCVD SiON deposition.

The other characteristics of LPCVD SiON films are generally favorable. LPCVD deposited SiON films have good index and thickness uniformity and good run-to-run reproducibility [17]. Worhoff et al. report the birefringence of an LPCVD SiON film (n=2.008) as 5×10^{-3} [27]. The amount of hydrogen incorporation during LPCVD deposition is much less than that incorporated during PECVD deposition. In LPCVD silicon nitride the total hydrogen content is approximately 4 at.%, while the hydrogen content in PECVD silicon nitride is about 22% [17]. The loss of slab type LPCVD SiON layers is below 0.2 dB/cm in the visible range [17].

2.2.3 Sputtered Silicon Oxynitride

Though only a limited amount of effort has been put into investigating sputtered silicon oxynitride for waveguide applications, sputtered silicon nitride and silicon oxynitride have been extensively studied for use in microelectronics and for anti-reflection coatings [32] [33].

Typically, silicon oxynitride is produced by reactively sputtering from a silicon target in an oxygen and nitrogen ambient [34] [35] [36]. Silicon nitride is typically sputtered reactively from a silicon target in a nitrogen ambient [103] [102]. A more comprehensive discussion of sputter processing is provided in Section 2.4.

2.3 Devices and Developments

There have been a number of devices produced using current silicon oxynitride technology. Additionally, there have been a number of developments and improvements in SiON waveguides. This section briefly outlines various devices and developments using current SiON processing technology.

Add-Drop Filters

A significant amount of research has gone into developing silicon oxynitride add-drop filters. These filters are an essential component of wavelength division multiplexing (WDM), allowing for the selection of specific channels. Particular attention has been given to developing wavelength tunable add/drop filters. Development of such filters will allow for reconfigurable WDM networks with dynamic wavelength allocation [37]. Add-drop filters also have applications as equalization filters, flattening the response of erbium doped fiber amplifiers [38]. Typically, add-drop filters are made using resonant couplers. These resonant coupler components consist of a number of directional couplers and optical delay lines [39, 40]. A typical add-drop component is shown in Figure 2.4. The spectral response of

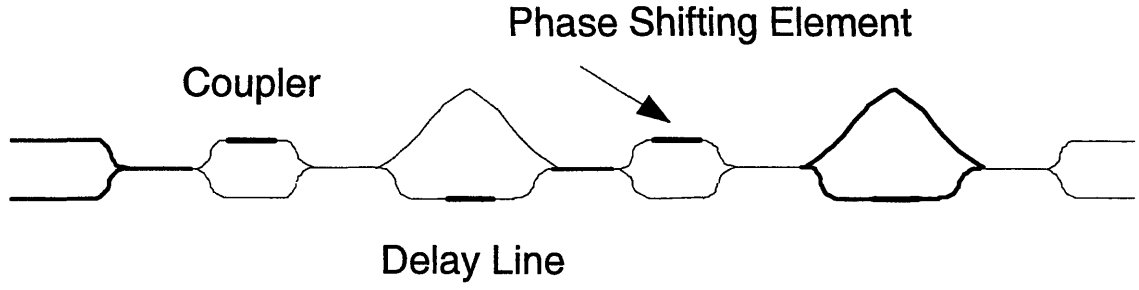

Figure 2.4: A resonant coupler component consisting of three tunable couplers and two tunable delay lines. Adapted from Offrein et al. [40].

this component is made fully adjustable by the use of heaters on all couplers and delay lines.

Silicon oxynitride has proven particularly useful for add-drop filter technology. Because of the large number of bends used in each RC component, the bending radius of silicon dioxide becomes prohibitive. The higher index, lower bending radius of SiON makes SiON ideal for use in add-drop filters [41]. Silicon oxynitride has been used to create splitters, 1-from-4, 1-from-8, and 1-from-16 add-drop filters [101, 42, 43, 44, 45]. Waveguide arrays have also been used to produce SiON themo-optical switches [48, 49].

Other Developments

The silicon oxynitride system has been used in developing other devices that address some of the other challenges inherent in creating an integrated optoelectronic technology. SiON has been used to develop spot size converters which reduce the coupling losses between

single mode silica fibers and single mode SiON waveguides [50].

Silicon oxynitride is also being used in amplifier development. SiON is being used as a host material for erbium in the development of erbium-doped amplifiers for optoelectronic applications [51].

Additionally, silicon oxynitride has demonstrated great promise for the development of low birefringence channel waveguides [52, 53]. Double core waveguides with a silicon nitride (n=2) birefringence compensating layer (BCL) below a SiON core are used to minimize waveguide birefringence.

2.4 Sputtering Physics

2.4.1 Overview

Sputter deposition is a physical deposition process in which a plasma is used to knock atoms of a target material which then deposit on a substrate. The plasma is created by applying a large voltage across a low pressure gas. The target material acts as the negatively charged cathode, the substrate as the positively charged anode. After a plasma is struck, positively charged plasma ions are accelerated toward the cathode target. As shown in Figure 2.5, a number of different events can happen when the energetic ions strike the target surface. If the ion energy is low enough, the ion may simply be reflected from the target. Alternately, if the ion energy is very high, the plasma ion may implant into the target, causing damage

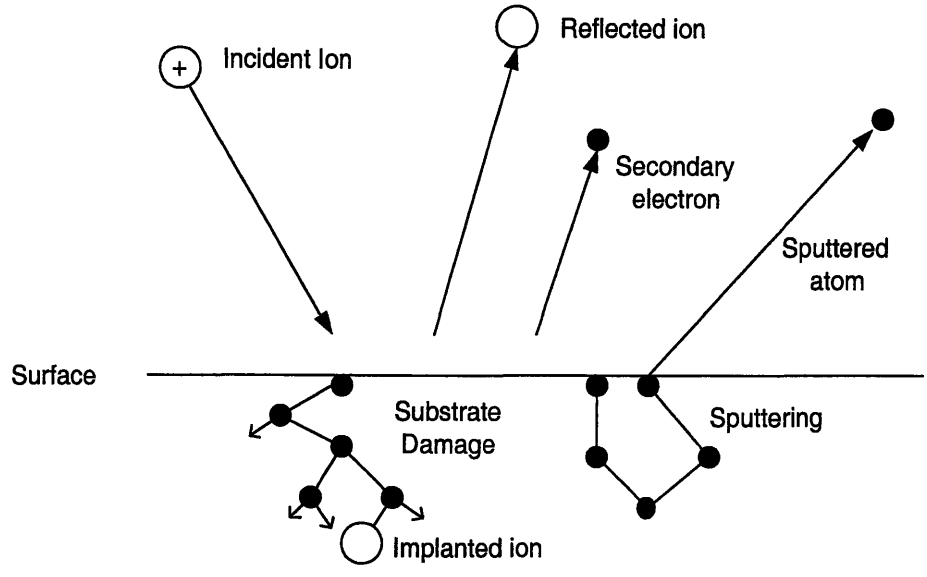

Figure 2.5: Sputtering Events. Adapted from Ohring [12]

to the substrate as it implants. Finally, at intermediate energies, the incident ion may travel several atomic layers into the target until it strikes a target atom; the incident ion then transfers its momentum to the target atom, and the target atom is rejected from the surface [13]. These ejected atoms are the atoms that provide for thin film deposition. Additionally, as the incident ions strike the target surface, they produce secondary electrons which are immediately accelerated away from the cathode. These electrons collide with the gas-phase atoms, and transfer energy to them. At lower energies, the electrons excite the atoms to higher energetic states. As the atom decays from the excited state to the ground state, the atom emits light, accounting for the characteristic plasma glow. At higher energies, the atoms ionize, and are accelerated towards the cathode region. In this manner, the plasma is maintained.

There are three basic types of sputter processes. The first is DC, or diode, sputtering. This process, described above, is used to efficiently deposit conducting materials. However, if we try to DC sputter an insulating target, we soon discover that it is impossible to draw the current necessary to produce a plasma [12]. In order to deposit from an insulating target, RF sputtering must be employed. At RF frequencies (typically 13.56MHz), electrons are driven by the varying electric field, and these electrons generate ions directly, reducing the voltage necessary to maintain a plasma [11]. Since the bias oscillates, both the target and substrate will sputter; however, reducing the area of the target relative to the substrate increases the relative voltage across the target, increasing the sputter rate of the target relative to the substrate.

Another type of sputtering, magnetron sputtering, is the type employed in this research. In magnetron sputtering, magnets are used to confine electrons to an area close to the sputtering target. Figure 2.6 shows a typical planar magnetron configuration.

The Lorentz force:

$$F = -e(\mathbf{v}X\mathbf{B}) \tag{2.1}$$

(where v is the velocity of the electron B is the magnetic field), confines the electrons to a circular path around the target [11]. All of the excited Ar is thus confined to a "racetrack" around the target; all target erosion takes place in this racetrack region. Magnetron sputtering produces high sputtering rates because each confined electron produces numerous ionization events while confined by the magnetron. Additionally, the magnetron configu-

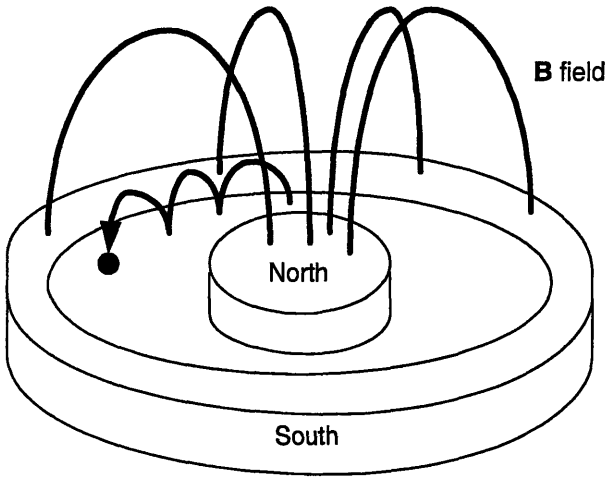

Figure 2.6: A typical planar magnetron configuration [11]

ration allows for a plasma to be maintained at a much lower pressure than in traditional dc and RF systems, further increasing the deposition rates achievable.

2.4.2 Sputter Processing Considerations

There are a number of concerns that must be considered when sputter processing. These considerations include sputter yield, atom energy and mean free path, and film uniformity. These considerations will be addressed in the following section with particular attention to the processing conditions used to deposit the SiON optical waveguides described in this thesis.

Sputter Yield

The yield from a single sputtering ion impacting a target is given as follows:

$$S = \frac{3\alpha}{4\pi^2} \frac{4M_1M_2}{(M_1 + M_2)} \frac{E_1}{E_b} \qquad (E_1 < 1keV) \tag{2.2}$$

where M_1 is the mass of the sputtering ion, M_2 is the mass of the target atom, E_1 is the energy of the sputtering ion, E_b is the surface binding energy of the target species, and α is a measure of the efficiency of momentum transfer [12]. (The parameter α increases monotonically from 0.17 to 1.4 as M_1/M_2 increases from 0.1 to 10 [12]). Figure 2.7 shows the variation of the mass term $\frac{4M_1M_2}{(M_1+M_2)}$ with target ion mass for Ar sputtering ions. Figure 2.7 demonstrates that the sputter yield of a mass 14 nitrogen atom will differ from that of a mass 28 silicon atom.

Although the two species sputter at a different rate, it is important to note that this does not mean that the amount of silicon sputtered off the Si_3N_4 target is greater than the amount of nitrogen sputtered off of the target. Initially, the rate of silicon sputtered is greater than the rate of nitrogen sputtered; however, the surface soon becomes depleted of silicon. As the surface becomes enriched with nitrogen, the rate at which the nitrogen sputters remains lower than the silicon sputter rate, but the amount of nitrogen available to sputter increases [12]. In this way, the stoichiometry of the sputtered species is maintained, even though the sputter yields of the two species are different. It is important to note that stoichiometry in the sputtered species does not necessarily guarantee stoichiometric film deposition becasue the sticking coefficients of the sputtered species may differ.

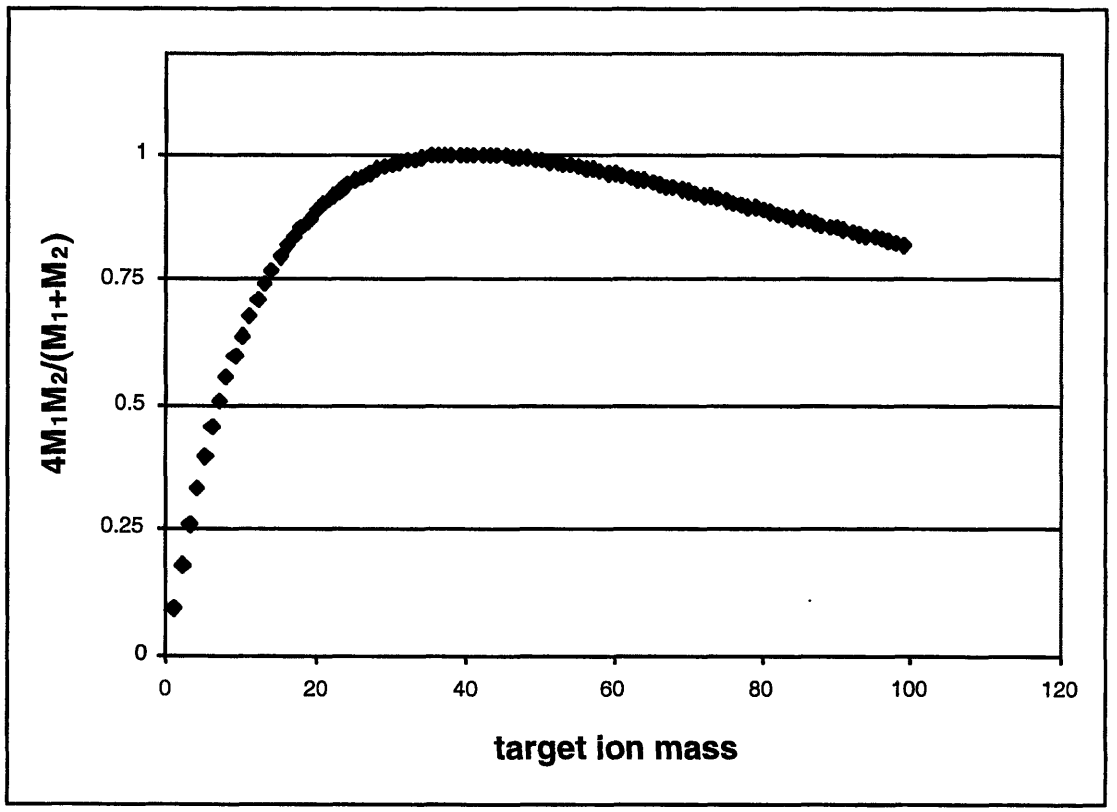

Figure 2.7: Sputter yield vs. target atom mass for atoms sputtered by Ar ions. Sputter yield is the yield from a single argon ion impacting a sputtering target.

Atom Energy and Mean Free Path

Understanding the mean free path (mfp) of molecules within the reaction chamber provides insight into the kinetics of the sputtering process. Following Ohring's development [12], we can consider each molecule in the reaction chamber to have a target area of $\pi(d_c)^2$, where d_c is the collision diameter of the molecule. To simplify, instead of considering the interaction of two molecules, both with a area d_c, we consider one molecule with a diameter of $2d_c$ and the other molecules as point sources. The distance that a molecule covers while traveling between collisions is then given as $\pi(d_c)^2\lambda_{mfp}$. A collision between molecules occurs when:

$$\pi d_c^2 \lambda_{mpf} n = 1 \tag{2.3}$$

where n is the number of molecules per unit volume. Kinetic theory also tells us that:

$$P = \frac{nRT}{N_A} \tag{2.4}$$

where R is the ideal gas constant and N_A is Avogadro's number. Combining equations 2.1 and 2.2, an expression for the mean free path can be derived:

$$\lambda_{mfp} = \frac{RT}{\pi(d_c)^2 N_A P} \tag{2.5}$$

The pressures in the sputtering chamber during deposition are approximately 1 mtorr (1 torr = 133.3Pa). Assuming a collision diameter of 5$\mathring{A}$, the mean free path of a molecule in the sputtering chamber is roughly 1 m. This means that a sputtered atom does not make any collisions before arriving on the substrate surface. Furthermore, in the case of reactive

sputtering, a sputtered atom does not collide with the reactive gas. This implies that there are no gas phase reactions in the sputtering chamber; the reactive gas can only react at the target surface or the substrate surface.

Film Uniformity

The thickness and index across a sputtered film is not uniform. All parts of the substrate are not an equal distance from the sputtering target. This variation in distance means that the flux of species arriving on the surface of the substrate varies across the surface of the substrate. The substrate is constantly rotated during deposition in order to moderate these distance effects. Figure 2.9 shows the variation in thickness for a variety of deposition conditions. Figure 2.8 shows the variation in index at 633 nm.

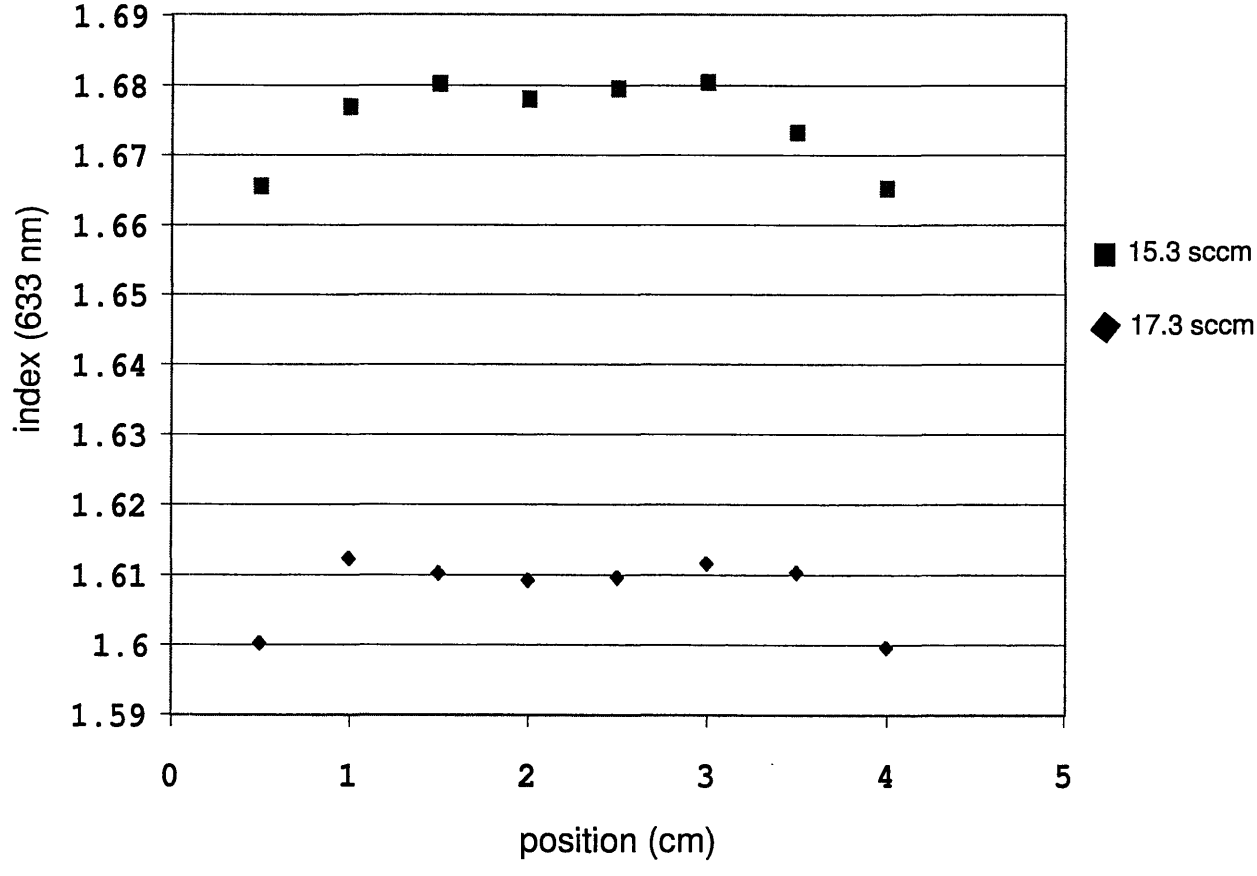

Figure 2.8: Uniformity of refractive index across a 4-inch Si wafer for samples deposited at 500 W and two different gas flow rates.

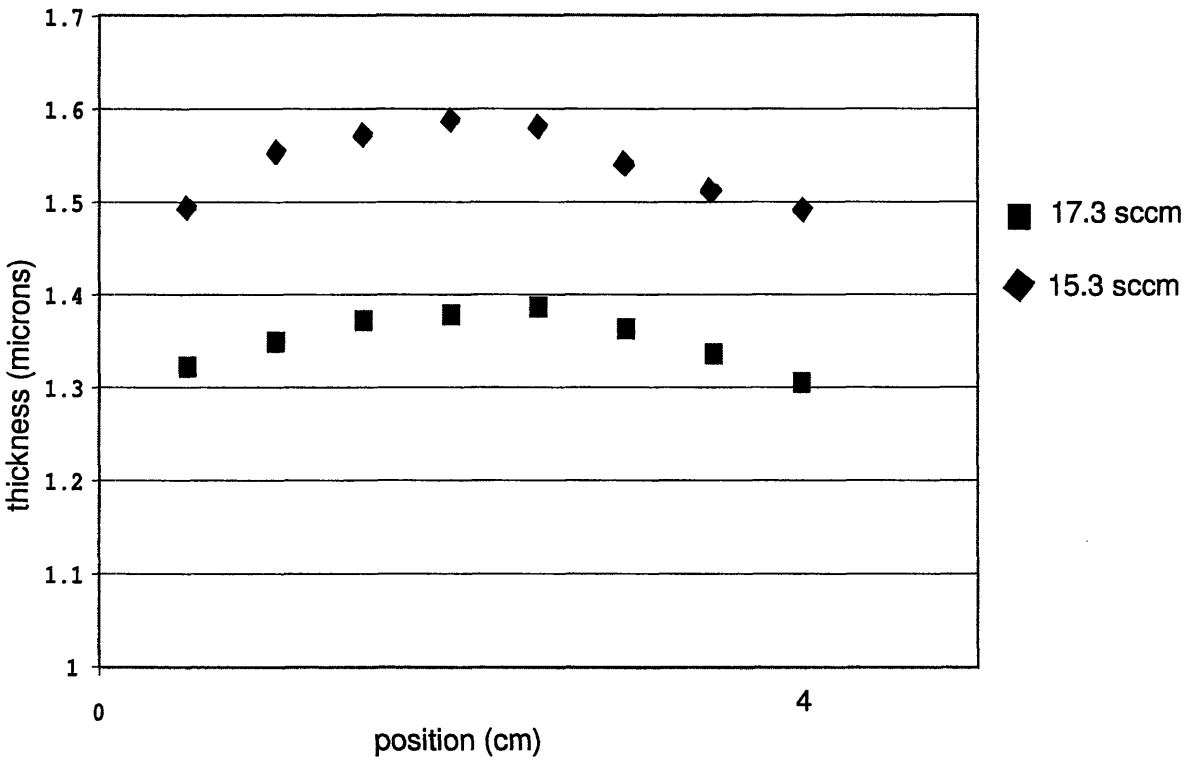

Figure 2.9: Uniformity of thickness across a 4-inch Si wafer for samples deposited at 500 W and two different gas flow rates.

Chapter 3

Model of Sputtering Process

This chapter provides the development of a model of reactive and cosputtered deposition of silicon oxynitride from dielectric sputtering targets. The chapter begins with a brief review of previous models of sputtered Si_3N_4 and SiON deposition. An introduction to residual gas analysis is provided, and, and RGA analysis is then performed on a number of reactive and cosputter depositions in order to understand the deposition products under a variety of processing conditions. Finally, a model is presented that predicts the composition and refractive index of cosputtered and reactively sputtered SiON films.

3.1 Previous Sputtering Models

The goal of this process modeling is to provide a model of the reactive and co-sputter depositions of silicon oxynitride from dielectric targets in order to understand the composition and optical properties of films deposited under various processing conditions (oxygen

partial pressure and target power). This understanding will ultimately allow us to tailor the processing of SiON films to the optical application.

There are a number of models given in the literature for reactive sputter deposition of silicon nitride and silicon oxynitride. A description of these models is given below. However, these reactive sputter deposition models are insufficient to describe the deposition processes described in this thesis.

The most comprehensive reactive nitride sputtering models come from Berg et al., who have extensively studied reactive sputter deposition of nitride compounds from a metal (or semiconductor) target in a reactive nitrogen ambient [109, 110, 111, 112, 113]. The main phenomenon modeled by the Berg group is that of the hysteresis present in sputtering rates vs. reactive gas mass flow when depositing under the above conditions. A sample hysteresis curve is shown in Figure 3.1. When reactive sputtering from a metal, there are two distinct deposition regimes [111]. The first occurs when the reactive gas concentration in the chamber is low. In this case, the sputter target surface is primarily composed of metal atoms, and the sputter rate is high. The second deposition regime occurs when the reactive gas partial pressure is high. In this case, the target surface becomes nitrided, and the sputtered material is now a dielectric. This dielectric sputtering produces the dramatic drop in sputter rates at high partial pressures, and the films deposited under these conditions are nitride-like.

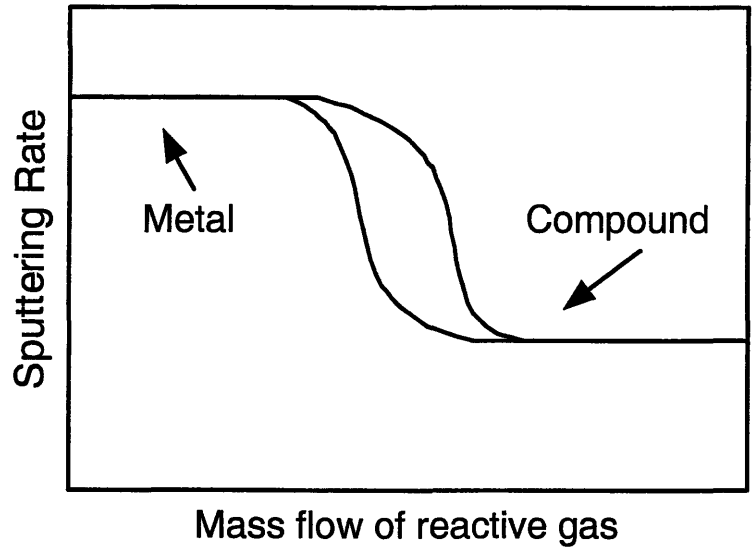

Figure 3.1: Schematic of the sputtering rate vs. reactive gas mass flow for reactive sputtering from a metallic target. Adapted from [111]

Berg et al. consider the steady state case of species depositing from a target partially covered in a nitride compound. At steady state, it is necessary that the compound errosion rate (which is a function of argon ion current) is equal to the compound formation rate (which is a function of the gas pressure in the chamber). Equating these two quantities allows Berg et al. to calculate the film deposition rate as a function of argon ion current and reactive gas partial pressure [109]. This model can be extended to predict film stoichiometry under certain processing conditions [111]. Stedile et al. have experimentally confirmed much of the Berg model with reactively sputtered silicon nitride [114].

Carlsson et al. expand upon the Berg model by analyizing reactive sputtering from a metal target using two reactive gasses. By adapting the Berg model, Carlsson provides simple

processing curves for oxynitrides reactively sputtered from a metallic target [112]. No compositional information is provided, however. Pinard Mackowski provide an alternative approach to reactive silicon oxynitride modeling (of SiON sputtered from Si in N_2 and O_2). Their model qualitatively predicts a linear variation of index with oxygen partial pressure and a decrease in refractive index at higher rf power.

Though the above models provide a good understanding of reactive sputtering from a metal-like target, they are not sufficient to describe the reactive sputtering process employed in this work. The main difference is that the reactive sputtering process we use to produce oxynitrides utilizes a dielectric silicon nitride target. Therefore, the metal-like to compound-like transition described above does not occur, and does not need to be considered. However, the following sections will show that dielectric sputtering is complicated by the fact that the dielectric silicon nitride does not sputter in stoichiometric ratios, and the oxidization behavior of the dielectric is not easily predictible. These factors must be fully understood before we can present a comprehensive model of our reactive silicon oxynitride process.

3.2 Residual Gas Analysis

3.2.1 Overview of Residual Gas Analysis

Residual gas analysis provides a method for identifying the gas species in the reaction chamber both before and during deposition. The residual gas analyzer (RGA) is mounted

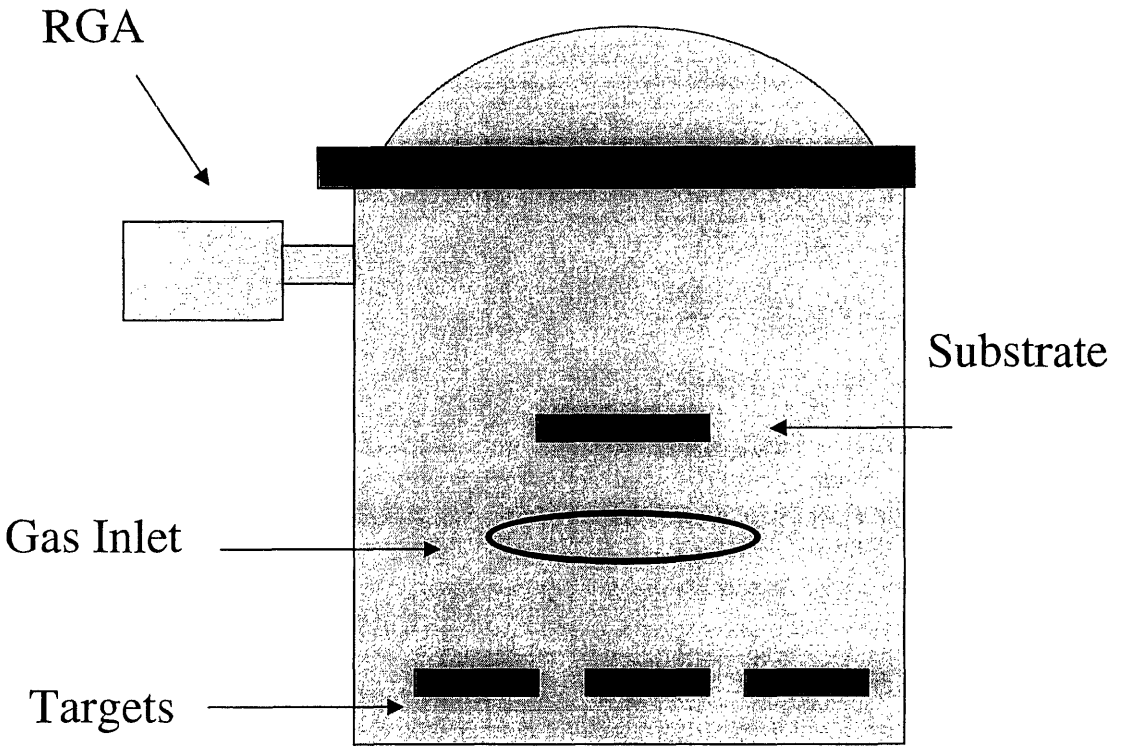

Figure 3.2: Schematic of sputter process chamber. Note the position of the RGA relative to the gas source and the targets.

as shown in Figure 3.2. It is important to note that the RGA is mounted far from the target, substrate, and gas inlets. The RGA is unable to monitor the actual reacting species in the chamber; instead, it measures products of the reaction that are able to diffuse from the area of the reaction up to the RGA. Though the RGA is unable to provide direct evidence of the sputter reactions taking place in the chamber, the indirect evidence that it provides can give good insight into the reactions taking place during the sputter process.

Residual gas analysis utilizes a mass spectrometer that measures the mass to charge ratio of

ions in the reaction chamber [105]. The majority of the species within a reaction chamber are neutral species. (The exception is within the plasma region, where there are a significant number of ions.) Because the reactor ambient consists primarily of neutral species, it is first necessary to ionize the gas species. Electrons are emitted from a hot wire filament which collide with the gas species, producing positive ions [105]. A quadrapole is then used to select ions of a particular m/e ratio [105]. The mass spectrometer scans over all m/e ratios of interest, and a profile of ion current versus m/e ratio is created.

When interpreting molecular spectra, it is important to consider that during analysis the molecules of a species will undergo various sorts of dissociations and ionizations [105]. Consider the spectrum for diatomic oxygen with a mass of 32.

If $e + O_2 = O_2^+ + 2e$, a m/e peak will occur at 32 amu.

If $e + O_2 = O_2^{++} + 3e$, a m/e peak will occur at 16 amu.

If $e + O_2 = 2O^o + e$, no peak will occur, since no charged species will have been created.

If $e + O_2 = O^o + O^+ + 2e$, a m/e peak will occur at 16 amu.

It is also important to consider the various isotopes of the molecule under analysis. Monatomic oxygen has isotopes with mass 16, 17, and 18 [106]. Therefore, in addition to a large 32 amu peak, diatomic oxygen will exhibit small peaks at 33, 34, 35, and 36 amu. Because of the various dissociations and ionizations these various isotopes can undergo, peaks (some

large and some quite small) will occur at 16, 17, 18, 32, 33, 34, 35, and 36 when O_2 is analyzed. Though the variety of mass peaks can initially add some confusion to RGA analysis, the next section will demonstrate that these secondary peaks can also be exploited to differentiate between the signals from two different species with the same primary atomic mass (Si and N_2, for example).

3.2.2 Process Analysis

This section addresses changes in residual gasses in the processing chamber under various processing conditions. Silicon nitride and silicon dioxide targets are sputtered from separately and together, and the process gas is switched from a pure argon environment to a 10% oxygen in argon gas mix.

Isotope Analysis

Before examining the RGA analysis of sputtered SiON deposition, it is necessary to establish which species are represented by what masses. Most importantly, it is important to be able to distinguish between a silicon signal and a diatomic nitrogen signal; both species have a (most abundant) mass of 28. In order to separate the silicon signal from the diatomic nitrogen signal, isotope analysis is employed. The relative abundance silicon and nitrogen isotopes are shown in Table 3.1.

The following chart shows the ion current signals of mass 28 and 29 collected during a silicon nitride deposition. The deposition was performed from a Si_3N_4 target; the flow rate of Ar was 7 sccm, and the power was varied as shown in Table 3.2.

Silicon		Nitrogen	
Mass 28	92.2%	Mass 14	99.6%
Mass 29	4.68%	Mass 15	0.37%
Mass 30	3.09%		

Table 3.1: Relative Abundance of Oxygen and Nitrogen Isotopes [106]

	100 W	200 W	300 W	400 W	500 W
Mass 28	$3.52x10^{-8}$	$5.77x10^{-8}$	$7.42x10^{-8}$	$8.67x10^{-8}$	$9.73x10^{-8}$
Mass 29	$2.87x10^{-10}$	$4.74x10^{-10}$	$6.07x10^{-10}$	$6.91x10^{-10}$	$7.75x10^{-10}$
% 28/29	0.081%	0.082%	0.082%	0.080%	0.080%

Table 3.2: RGA ion currents of silicon and nitrogen-associated masses.

This chart demonstrates that for all powers the mass 29 signal is about 0.8% of the mass 28 signal. The isotope ratios demonstrate that if these signals were entirely from nitrogen, mass 29 would be about 0.4% of the mass 28 signal. Conversely, if silicon were the only contributor, the 29 peak would be 5.08% of the 28 peak. The experimentally determined mass ratios show that the mass 28 peak primarily nitrogen, and about half of the signal observed at mass 29 is caused by silicon and about half caused by nitrogen. Of course, the nitrogen signal at 29 actually represents a much larger amount of nitrogen than does the silicon signal, since the abundance of mass 29 nitrogen is less than 10% of mass 29 silicon. (In order to determine the exact contributions of silicon and nitrogen, we have to know the ionization behavior of both species in our particular system. In fact, we do not know these behaviors, and therefore cannot calculate the relative abundance of silicon to

nitrogen exactly.)

Gas Analysis

The following graph shows the evolution of the residual gas profile in the chamber as the gas mixture and sputtering targets are gradually varied. The target/gas combination at each step is shown in Figure 3.3.

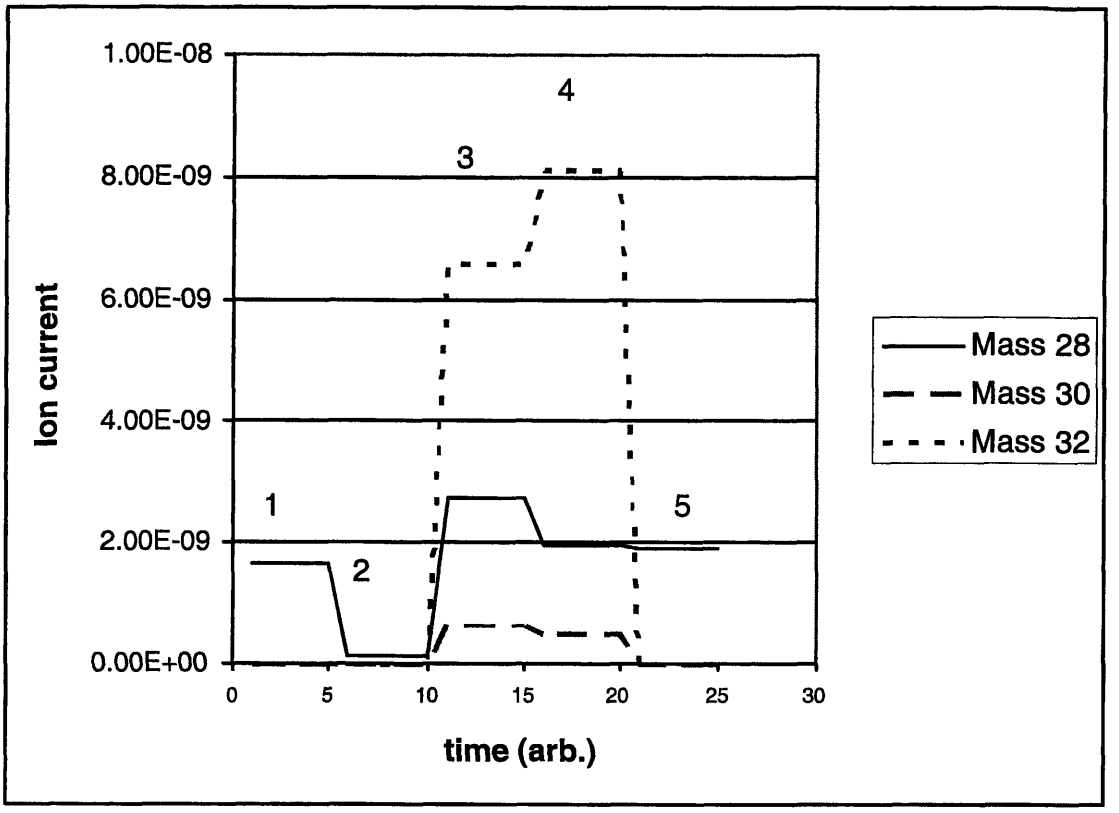

Figure 3.3: Variations of ion current with processing condition

1a. Si_3N_4 (100 W) in Ar (20 sccm)

2a. Si_3N_4 (100 W) and SiO_2 (100 W) in Ar (20 sccm)

3a. Si_3N_4 (100 W) and SiO_2 (100 W) in 10%O_2/90%Ar (20 sccm)

4a. Si_3N_4 (100 W) in O_2/Ar (20 sccm)

5a. Si_3N_4 (100 W) in Ar (20 sccm)

The same progression, only starting with the oxide target is shown in Figure 3.4.

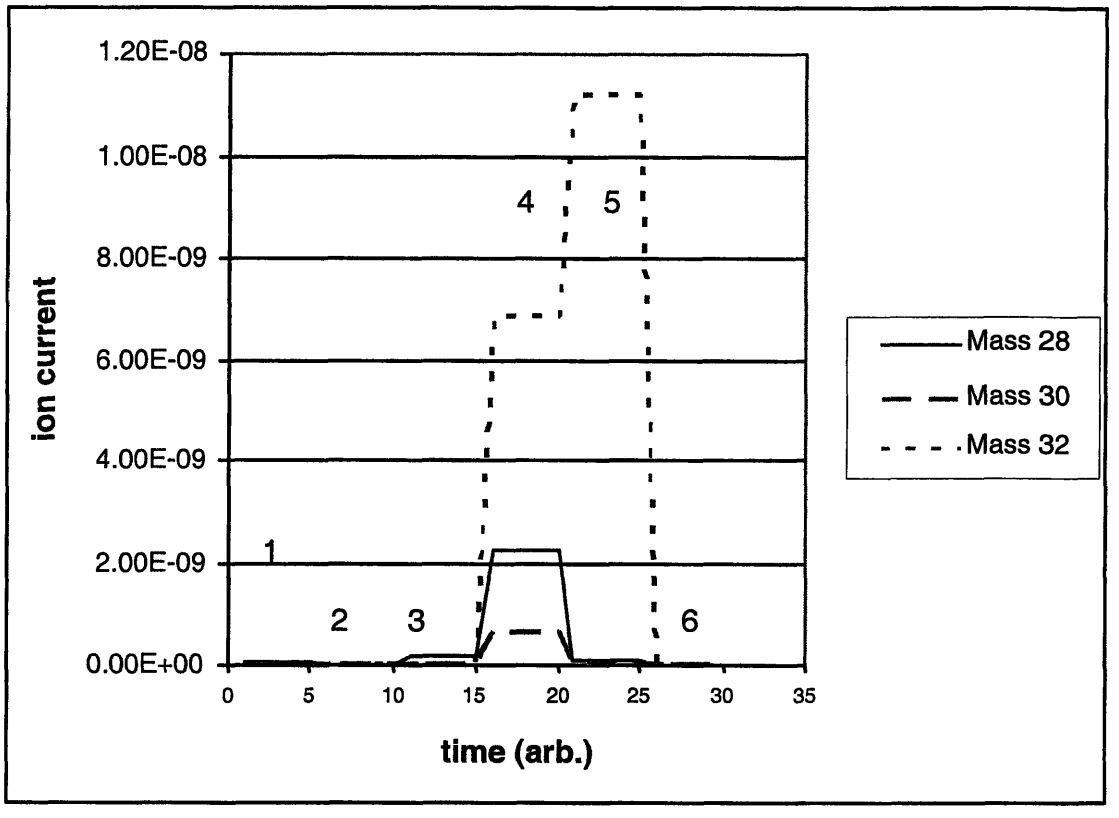

Figure 3.4: Variations of ion current with processing condition

1b. no target, Ar (20 sccm)

2b. SiO_2 (100 W) in Ar (20 sccm)

3b. SiO_2 (100 W) and Si_3N_4 (100 W) in Ar (20 sccm)

4b. SiO_2 (100 W) and Si_3N_4 (100 W) in 10% O_2/90% Ar (20 sccm)

5b. SiO_2 (100 W) in O_2/Ar (20 sccm)

6b. SiO_2 (100 W) in Ar

From the above gas profiles, we can write several reaction mechanisms that show the gas species evolved from the target during deposition. All other species evolved from the target are assumed to be incorporated into the depositing film. Please note that all oxidation reactions are assumed to take place on the surface of the silicon substrate. However, the sputtering setup employed allows oxygen to diffuse to the target surface as well; therefore, oxidation reactions may also take place at the target surface, and the product oxide may be sputtered to the substrate. The gas flow setup of the sputtering machine used in this research necessitates flowing in both argon and oxygen away from the target surface. In the future, altering the gas flow setup to localize the argon flow to the target surface may help restrict the oxidation reactions to the substrate surface.

Starting with the depositions in argon:

Reaction in argon plasma

Silicon Dioxide

Analysis 2b shows the reaction of silicon dioxide in argon. It demonstrates that no free gas products are formed. We can write:

SiO_2(target) —> SiO_2(film)

Silicon Nitride

The reaction of the Si_3N_4 target is a bit more complicated. Reaction 1a shows nitrogen

in argon plasma. There is a significant amount of free nitrogen detected by the RGA during this reaction. There is also a peak at mass 29 that is 0.74% of the mass 28 peak; this indicates that only a small amount of free silicon is liberated along with a substantial amount of nitrogen. This would indicate that films deposited from a silicon nitride target in an argon plasma should be silicon rich.

$Si_3N_4(target) \longrightarrow Si_3N_{4-\delta}(film) + N_2(g)$

Silicon Dioxide and Silicon Nitride

Both 3b and 2a represent cosputtering from SiO_2 and Si_3N_4 in an argon plasma. The complete reaction does not form any free product. However, since we know that the silicon nitride sputtering process produces a nitrogen byproduct, we can conclude that that the silicon dioxide target serves to getter free nitrogen from the atmosphere, likely because the additional silicon from the SiO_2 target aids in nitrogen gettering. The overall reaction and the sub-reactions that take place are written below. We can conclude that the SiO_2/Si_3N_4 cosputtered films are likely to be stoichiometric since there is no residual gas product from the reaction.

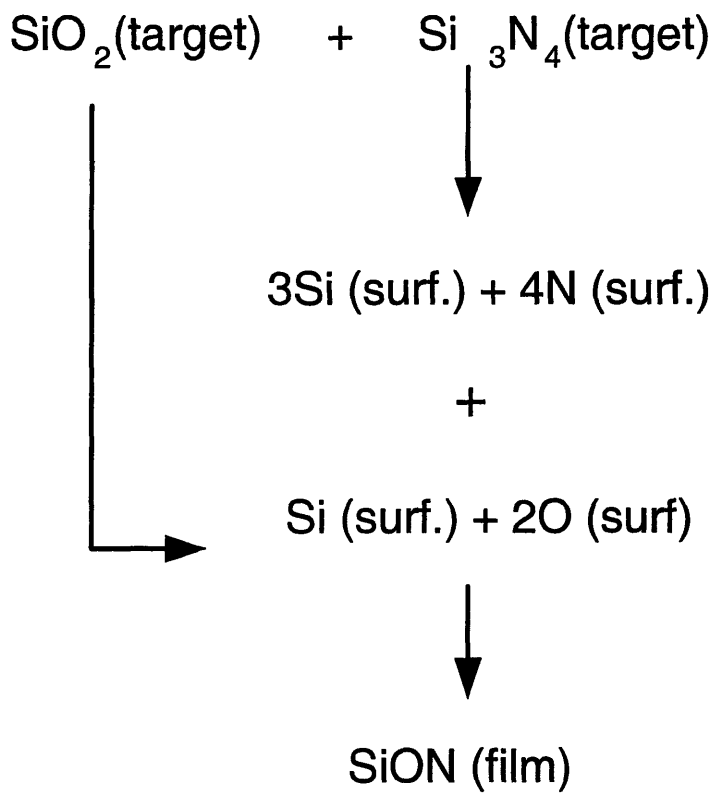

Silicon Nitride in Oxygen

This sputter process produces a rise in a number of gas products. An excess of both nitrogen and N-O (mass 30) are observed in the chamber. Since excess nitrogen is liberated during this sputter process, we would expect that these films would also be nitrogen deficient.

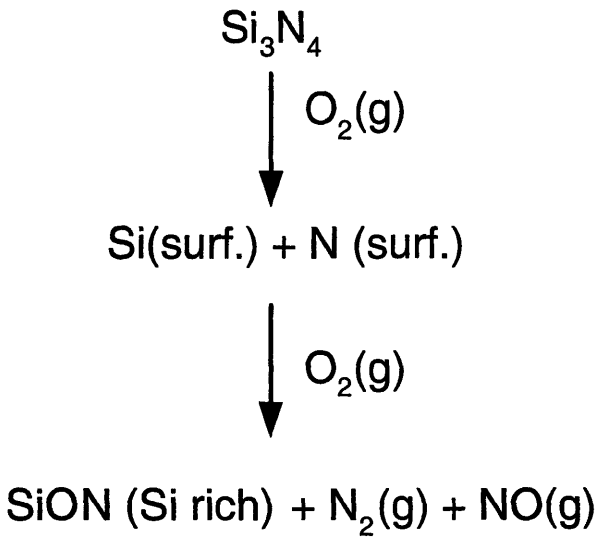

Summary of RGA Analysis:

The above analysis demonstrates that the co-sputtered oxynitride films evolve very little gas into the atmosphere. This low gas evolution indicates that the stoichiometry of the co-sputtered oxynitride is very good, since all of the sputtered species are being incorporated into the film in the correct proportions. The reactively sputtered oxynitride and the sputtered nitride show a different gas profile. The reactively sputtered oxynitride films evolve both nitrogen and N-O species into the chamber during sputtering. The sputtered silicon nitride gives off nitrogen into the reaction chamber. The RGA analysis predicts that the sputtered silicon nitride films will be silicon rich. The reactively sputtered oxynitride are predicted to be silicon rich (if the excess silicon is not completely reacted by the ambient oxygen) or stoichiometric (if the ambient oxygen satisfies all of the excess silicon).

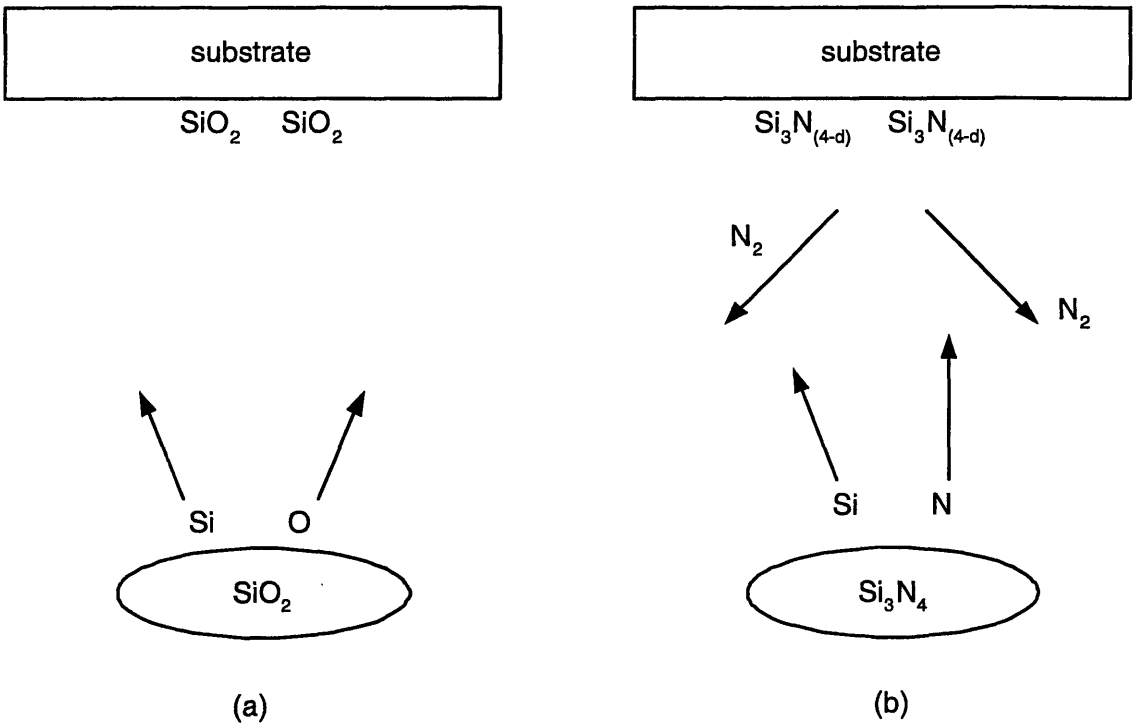

Figure 3.5: Schematic contrasting (a) sputtering from an oxide target with (b) sputtering from a nitride target. In the case of the oxide, all of the sputtered species incorporate into the depositing oxide film. In the case of the nitride, some of the nitrogen forms diatomic nitrogen which desorbs from the film surface, leaving a nitrogen depleted film behind.

3.3 Silicon Oxynitride Sputtering Models

3.3.1 Sputtering from a Dielectric Target

As the previous sections demonstrate, sputtering from a silicon dioxide target produces a film with much better stoichiometry than sputtering from a silicon nitride target. Figure 3.5 contrasts silicon dioxide sputtering with silicon nitride sputtering.

In order to explain the difference between silicon dioxide sputtering and silicon nitride sputtering, it is necessary to consider the bond energies of the relevant diatomic species. Table 3.3.1 gives bond enthalpies for various silicon, oxygen, and nitrogen diatoms.

Bond	kJ/mol
O-O	498.36
N-N	945.33
Si-O	799.6
Si-N	470

Table 3.3: Bond enthalpies of silicon, oxygen and nitrogen diatomic species

Table 3.3.1 shows that the bond strength of a Si-O bond is much higher than the bond strength of a O-O bond. Conversely, this figure shows that the bond strength of a N-N bond is much stronger than the bond strength of a Si-N bond. This difference in bond strength clearly indicates that the formation of N-N bonds during deposition from a silicon nitride target is far more favorable than the formation of O-O bonds during the deposition from a silicon dioxide target.

When sputtering from a silicon nitride target in an oxygen ambient, the formation of N-N bonds remains highly favorable. In fact, because Si-O bonding is more energetically favorable than Si-N bonding, the presence of an oxygen ambient serves to eject even more diatomic nitrogen species into the ambient. However, because the ambient oxygen is available to react with the excess silicon in the depositing film, reactively sputtered silicon

oxynitride films are generally higher quality than silicon nitride films deposited in Ar only.

3.3.2 Cosputtering from SiO_2 and Si_3N_4

From the RGA analysis described in the previous section, we can conclude that there is little O_2 and N_2 gasses liberated when cosputtering SiON from SiO_2 and Si_3N_4. If a homogeneous alloy of oxide and nitride is assumed, the following reaction can be written for the formation of silicon oxynitride:

$$xSi_3N_4 + ySiO_2 - - > Si_{3x+y}O_{2y}N_{4x} \tag{3.1}$$

The index of refraction of cosputtered silicon oxynitride can then be written as:

$$n_{SiON} = f_{SiO_2} n_{SiO_2} + (1 - f) n_{Si_3N_4} \tag{3.2}$$

where n_{SiON} is the refractive index of SiON at a given composition, f_{SiO_2} is the mole fraction of SiO_2 in the SiON, and n_{SiO_2} and $n_{Si_3N_4}$ are the refractive indicies of stoichiometric SiO_2 and Si_3N_4, respectively. The use of the stoichiometric indices of SiO_2 and Si_3N_4 is justified by the RGA data, where little gas evolution is observed in the cosputtered process which could contribute to non-stoichiometry.

The fraction f of SiO_2 and Si_3N_4 deposited on the substrate is proportional to the power applied to the oxide and nitride targets, respectively. Empirically, the deposition rate of

SiO_2 has been shown to be about 0.75 that of Si_3N_4 at equal powers. Thus, we can write the refractive index as a function of target power:

$$n_{SiON} = \frac{0.75P_{SiO_2}}{0.75P_{SiO_2} + P_{Si_3N_4}} n_{SiO_2} + \frac{P_{Si_3N_4}}{0.75P_{SiO_2} + P_{Si_3N_4}} n_{Si_3N_4} \tag{3.3}$$

where P_{SiO_2} is the power applied to the silicon dioxide target, and $P_{Si_3N_4}$ is the power applied to the silicon nitride target.

Figure 3.6 shows the predicted variation of refractive index with target power. The experimentally determined data show a good match with theory. This theoretical prediction is expected to be best when the flux of SiO_2 is large compared to the flux of Si_3N_4. At lower oxide fluxes, there may not be enough excess silicon available to getter all of the free nitrogen, resulting in a somewhat nitrogen deficient alloy.

3.3.3 Reactive Sputtering from a Si_3N_4 Target in an O_2 Ambient

Reactive Oxygen Incorporation

The reactive sputtering process is somewhat more complicated than the cosputtering process described above. Before we can predict the refractive index of these sputtered films, we must understand the reactive gas profiles in the chamber under different processing conditions. This section describes the different regimes governing oxygen gettering during the reactive sputter process.

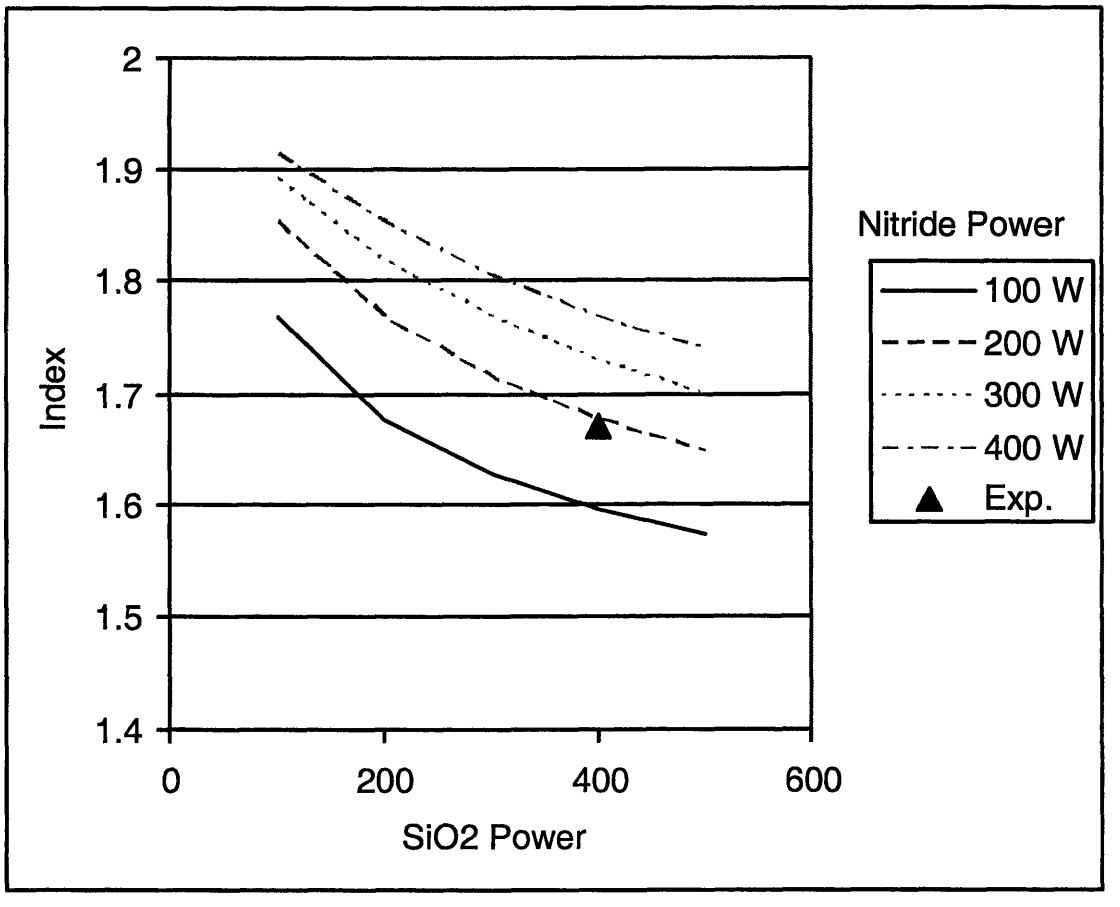

Figure 3.6: Predicted and experimental values of refractive index at various nitride and oxide target powers.

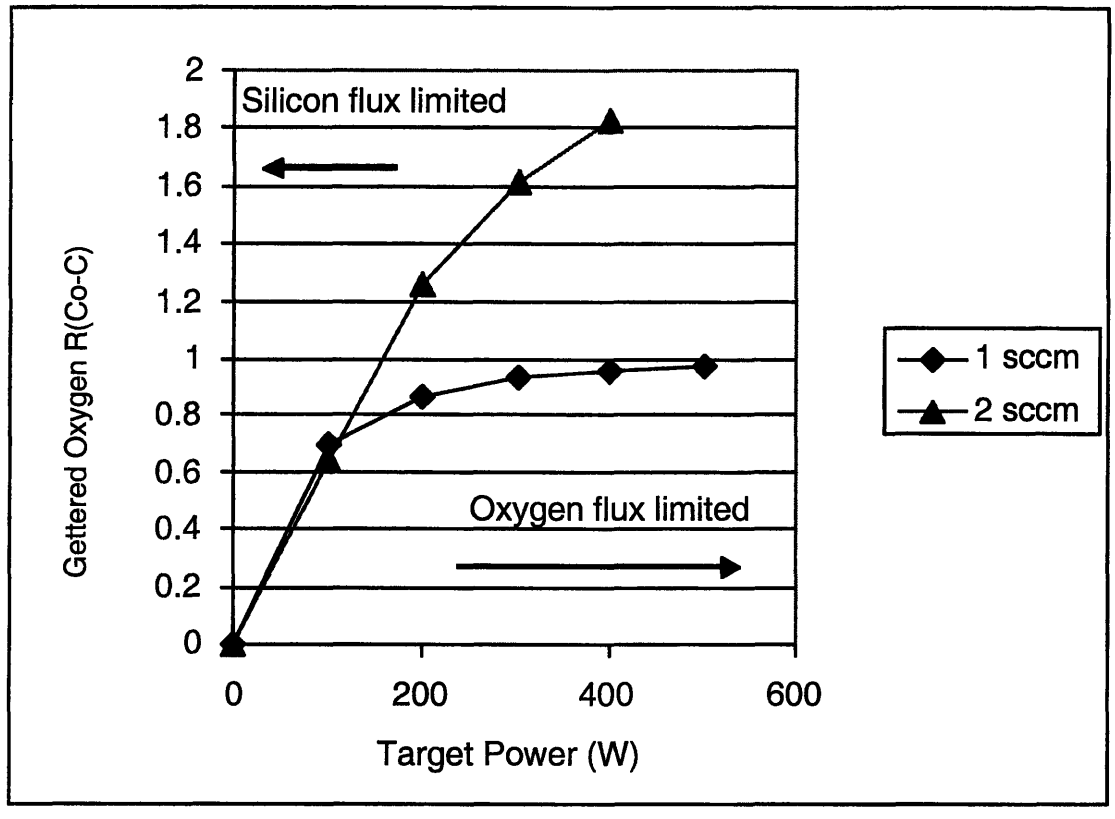

Figure 3.7: Gettered Oxygen vs. power for gas flows of 1 sccm O_2 and 2 sccm O_2 during reactive sputtering process. Solid lines are provided to guide the eye.

Figure 3.7 describes the oxygen incorporation in SiON films reactively sputtered from Si_3N_4 in an O_2 ambient at various powers. The initial concentration of oxygen in the reaction chamber is given by C_o, and R is the rate of oxygen flow into the chamber in sccm. In all cases, the initial concentration of oxygen in the process gas, and therefore in the reaction chamber, is 10an RGA, and $R(C_0 - C)$ is plotted as a function of power in Figure 3.7 for two different gas flow rates. The difference $R(C_0 - C)$ represents the amount of oxygen gettered into the depositing film.

The oxygen incorporation during reactive sputtering can be described as follows:

1.) Silicon nitride is sputtered from a Si_3N_4 target. In previous sections, we established that silicon nitride does not sputter in stoichiometric ratios. Rather, nitrogen gas is liberated into the reaction chamber, and a silicon-rich film is deposited.

2.) In a reactive environment, this silicon reacts with the ambient oxygen. Additionally, the oxygen can compete with the nitrogen to react with the silicon.

The oxidation reaction can be written as:

$$Si + O_2 - - > SiO_2 \tag{3.4}$$

3.) If the flux(O_2 to the film surface) >> flux(O_2 incorporating into the film), the following analysis will be valid.

4.) The flux of oxygen incorporating into the film (F_{film}), is given by:

$$F_{film} = kC_{Si} \tag{3.5}$$

where k is the chemical reaction rate constant for the oxidation process, and C_{Si} is the concentration of Si available to react with the oxygen.

5.) The amount of oxygen gettered into the depositing film is will then be equal to this flux multiplied by the area of the wafer (A), the deposition time (t), and a sticking coefficient

(α) which will be assumed independent of C_{Si}. For further discussion of the oxygen sticking coefficient, please see the next section. The amount of gettered oxygen can therefore be written as:

$$[O] = \alpha k C_{Si} A t \tag{3.6}$$

The above analysis predicts that the amount of oxygen incorporated into the film should vary linearly with the amount of silicon on the substrate surface. Figure 3.8 shows that the amount of nitrogen liberated from the target can be approximated as varying linearly with power over the 100-500W power range. Therefore, the amount of oxygen incorporated into the depositing film should be expected to vary linearly with power.

Figure 3.7 shows that at lower powers, the amount of gettered oxygen does in fact vary linearly with power. At low powers, the flux of oxygen to the substrate surface is much greater than the flux of silicon to the substrate surface, and the amount of oxygen reacted is limited by the number of silicon sites available with which to react. In this silicon flux-limited regime, we see that the amount of gettered oxygen is independent of the rate of oxygen flow into the reaction chamber. Section 3.3.4 describes the reactive sputtering in this oxygen flux-limited regieme.

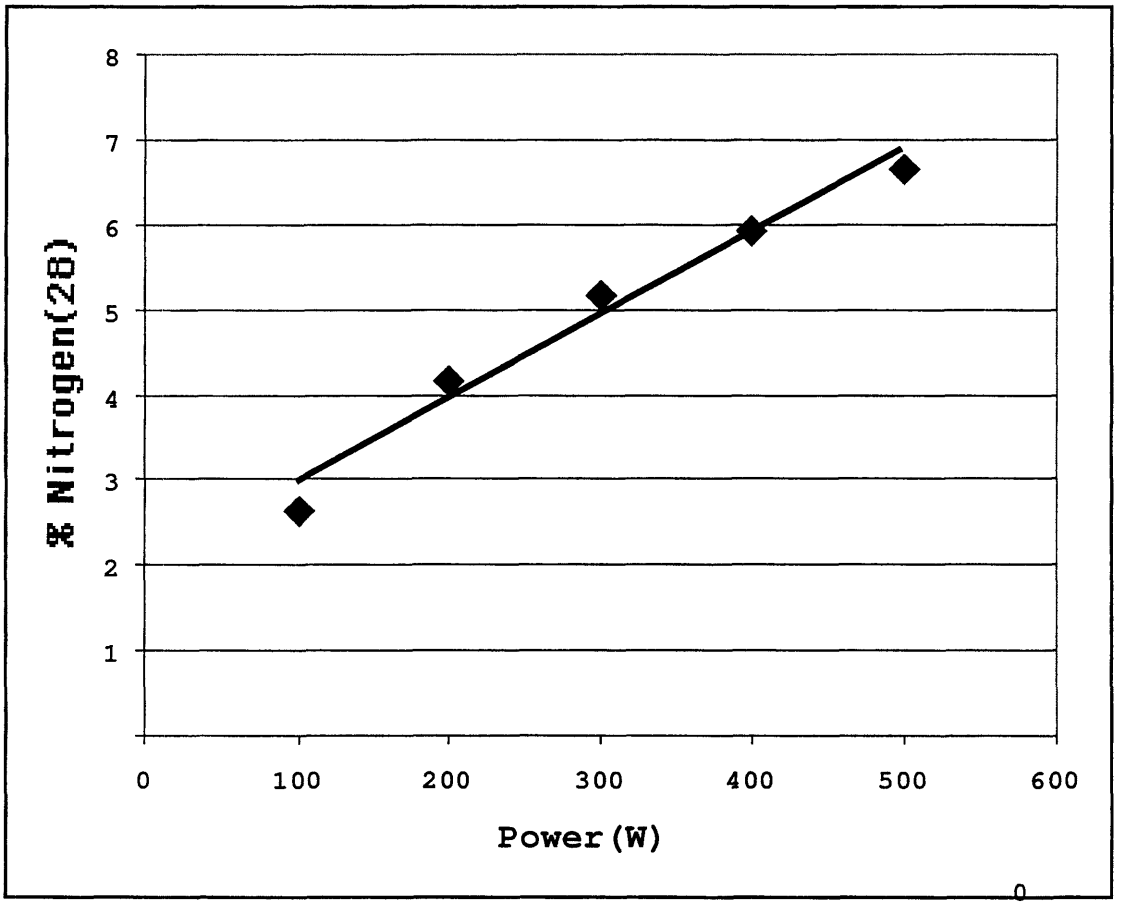

Figure 3.8: The variation of nitrogen (mass 28) content in reaction chamber vs. Si_3N_4 target power.

3.3.4 Model of Reactive Sputtering of SiON

From the RGA analysis described in the previous section, the SiON-forming reaction can be written as:

$$Si_3N_4 + zO_2 - - > SiO_{2x}N_{(1-z)} + N_2 \tag{3.7}$$

This reaction is vaild for reactions in the O_2-limited regime, where the vast majority of the oxygen in the reaction chamber is gettered into the depoisting film. The index of refraction of the sputtered SiON film can the be written as a linear combination of the indices of SiO_2 and SiN. (The index of the silicon-rich sputtered Si_3N_4 is determined by prism coupling to be 2.3. This index indicates a Si-rich silicon nitride alloy consisting of 18% Si. This stoichiometry closely resembles that of SiN.)

$$n_{SiON} = f_{SiO_2} n_{SiO_2} + f_{SiN} n_{SiN} \tag{3.8}$$

However, in order to compare this result to the experimentally determined indicies, it is necessary to write the index in terms of fluxes, instead of mole fractions. The ratio of fluxes can be written as:

$$\phi = \frac{\phi_{O_2}}{\phi_{Si_3N_4}} \tag{3.9}$$

where ϕ_{O_2} is the flux of diatomic oxygen to the substrate surface, and $\phi_{Si_3N_4}$ is the flux of Si_3N_4 to the substrate surface. Adjusting for the fact that silicon nitride deposits as SiN, we can write:

$$n_{SiON} = \frac{\phi}{3.5+\phi} n_{SiO_2} + \frac{3.5}{3.5+\phi} n_{SiN} \tag{3.10}$$

This theoretical prediction of refractive index is shown as the solid line in Figure 3.9.

In order to compare this theoretical predition to the experimentally determined numbers, it is necessary to write the index of refraction as a function of the flux of Si_3N_4 and O_2. The following proceedure is used to determine these two fluxes:

- The deposition rate of Si_3N_4 at 500 W (7sccm Ar) has been determine to be 8.8x10^{-5} μm/sec using profilometry. If we assume that the deposition rate is linear with power, the deposition rate of Si_3N_4 at 400 W can be approximated as 7.4x10^{-5} μm/sec.

- The density of Si_3N_4 is 1.48x10^{22} molecules/cm^3. From the above flux data, we can then calculate the flux of molecules to be 1.32 x 10^{14} molecules/cm^2 at 500 W, and 1.11x10^{14} molecules/cm^2 at 400 W.

- The flux of oxygen molecules to the surface of the substrate can also be calculated. This flux is given as $F_{O_2} = \frac{p_{O_2}}{\sqrt{2\pi k_b T M}}$, where p_{O_2} is the partial pressure of oxygen in the chamber, k_b is the Boltzmann constant, T is the temperature, and M is the mass of the gaseous species. The total gas pressure in the chamber at 20sccm flow is measured to be 1 mtorr. The gas pressures at the other flow rates are linearly extrapolated from this pressure. This total gas flux, however, does not represent the oxygen flux to the substrate surface. The process gas is composed of only 10% O_2 in Ar. Additionally, a large portion of the oxygen

is gettered within the chamber, further reducing the flux of oxygen to the substrate surface. Table 3.3.4 gives the total flux of all gaseous species, the percent of O_2 species as measured by RGA, and the flux of O_2 onto the substrate surface.

Flow (sccm)	Power	% O_2	O_2 Gas Flux
20	500 W	0.836 %	3.0×10^{15}
17.3	500 W	0.793 %	2.46×10^{15}
15	500 W	0.676 %	1.82×10^{15}
13.3	500 W	0.59 %	1.41×10^{15}
10	500 W	0.238 %	4.27×10^{14}
17.3	400 W	0.793 %	2.46×10^{15}
10	400 W	0.421 %	7.55×10^{14}

Table 3.4: Calculated flux of oxygen to the substrate surface at various chamber pressures

The O_2 fluxes shown in Figure 3.3.4 are plotted against the experimentally determined indices of refraction in Figure 3.9. This figure shows that the theoretical prediction provides a very good match with experiment and allows for the prediction of refractive index under all O_2-flux limited deposition conditions. Figure 4.1 translates these fluxes into gas flow, and shows the actual and expected variation of index with gas flow rate at 400 and 500 W.

3.3.5 Model Summary

This chapter has presented two models for sputter deposition of silicon oxynitride. The cosputtering model shows that sputtering from a silicon nitride target and a silicon oxide

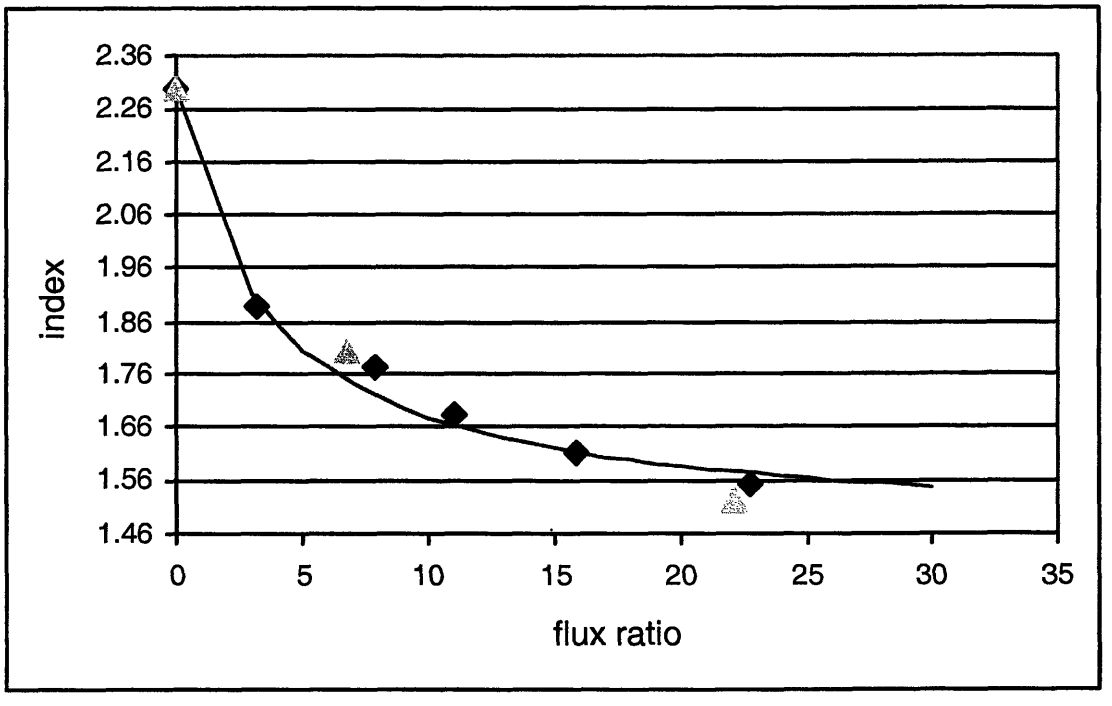

Figure 3.9: Theoretical prediction and experimental measurement of index vs. flux ratio at various flux ratios. ($\triangle$ = 400 W, $\Diamond$ = 500 W, solid line is theoretical prediction.)

target allows silicon oxynitride to be deposited with little oxygen or nitrogen gas evolution into the reaction chamber. This model allows us to easily predict the index and composition of the sputtered silicon oxynitride as a simple alloy of Si_3N_4 and SiO_2.

The reactive sputtering model presented describes a more complicated sputtering process. In the reactive case, silicon oxynitride is sputtered from a silicon nitride target in an oxygen ambient. Figure 3.10 summarizes this reactive sputtering process.

Silicon and nitrogen atoms arrive on the substrate surface from the sputtering target. Some of the nitrogen arriving on the substrate surface combines to form N_2, and this N_2 is ejected into the reaction chamber. The ambient oxygen also competes with the nitrogen to oxidize the silicon on the substrate surface. In the oxygen flux limited case, the oxygen content of the film can be easily adjusted, since nearly all of the ambient oxygen is incorporated into the depositing film.

Together, these models provide a method for accurately predicting the index of refraction of SiON sputtered under a wide variety of processing conditions. In Chapter 4, we will show that despite the complexity of the reactive sputter process, the reactive sputter model can also be used to predict the composition of the sputtered SiON. This model will be applied throughout the remainder of this thesis to predict the properties of films for both passive and active microphotonic device applications.

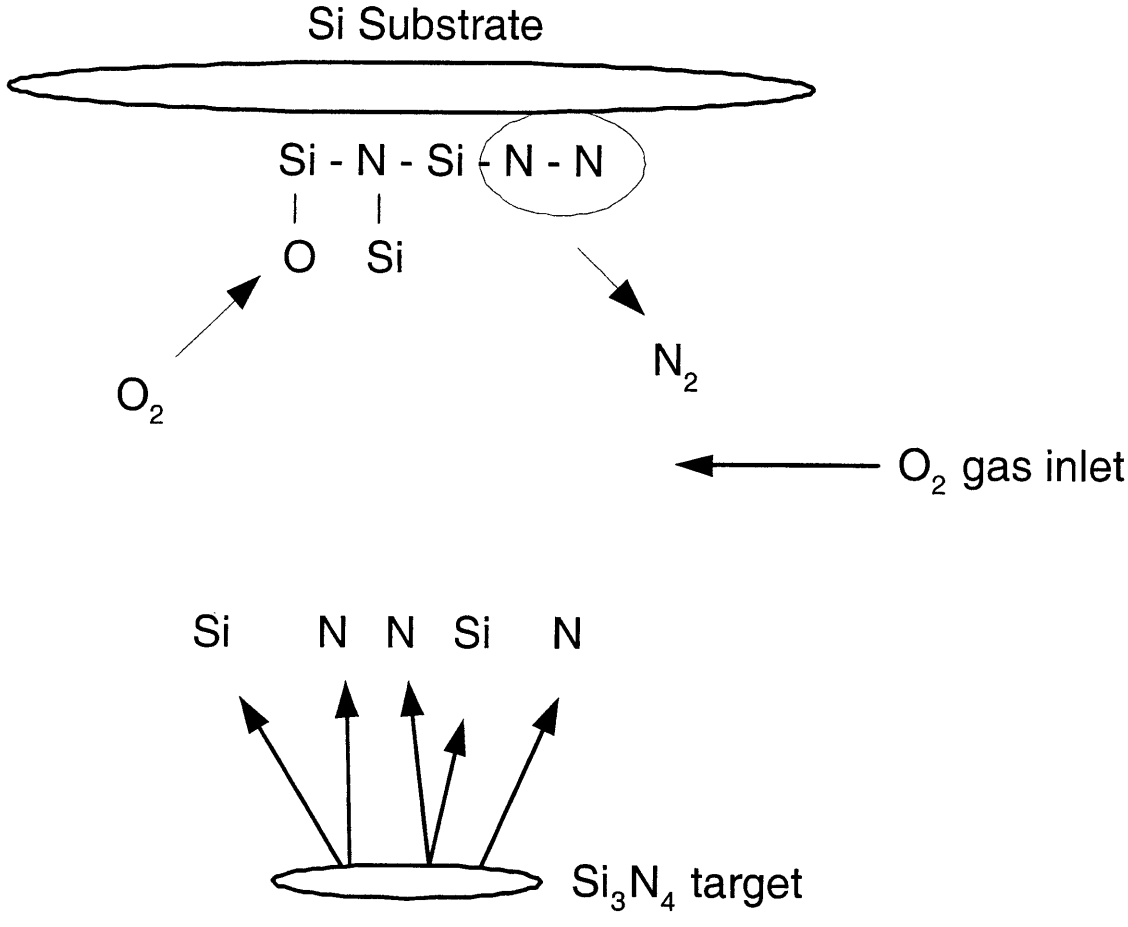

Figure 3.10: Description of the reactive sputtering of SiON from Si_3N_4 in O_2.

Chapter 4

SiON/Si_3N_4 Materials Analysis

This chapter begins with a brief overview describing the sputter process used to fabricate all of the films investigated in this thesis. A variety of film characterization techniques are then utilized to provide information about the refractive index, roughness, stress, composition, and bonding of the films. Many of the materials assumptions made in the first chaper are verified, and the film properties are evaluated from an optical waveguide perspective.

4.1 Processing Overview

Silicon oxynitride and silicon nitride are deposited using a Kurt J. Lesker sputtering system. The depositions were done from dielectric targets using RF-magnetron guns. The base pressure in the reaction chamber was on the order of $1x10^{-8}$ torr and the deposition pressure is typically less than or equal to 1 mtorr. An argon plasma was employed. Silicon nitride was sputtered directly from 3-inch silicon nitride target. Silicon oxynitride was either

reactively sputtered from a silicon nitride target in an oxygen ambient, or SiON was co-sputtered from a silicon nitride and a silicon dioxide target. Depositions were performed onto an unheated substrate, and the substrate was unbiased during deposition.

4.2 Film Characterization

4.2.1 Refractive Index Tuning

In order to fully exploit the silicon oxynitride materials system, it is necessary to be able to tune the refractive index of the SiON materials system over the full range of available indices. Figure 4.1 shows the variation of refractive index with gas flow rate (10% O_2 in Ar in reactively sputtered SiON. The solid lines show the index as predicted by the theory given in Section 3.3.4. The points, which show a good match to theory, are experimental.

Figure 4.1 demonstrates that we can tune the refractive index of sputtered SiON over a wide range of indices. Additionally, this figure shows that the index varies linearly with gas flow rate, which makes the refractive index easy to tailor. This refractive index can be easily predicted from the processing conditions using the method shown in Section 3.3.4. As predicted, the refractive index also varies with target power; the slower sputtering rates at lower powers allow for additional incorporation of oxygen, making the SiON more SiO_2-like, and lowering the refractive index. However, there is little change in the index of the sputtered silicon nitride film with power because there is no oxygen incorporation during deposition. The elevated index of the sputtered Si_3N_4 films indicates that these films are

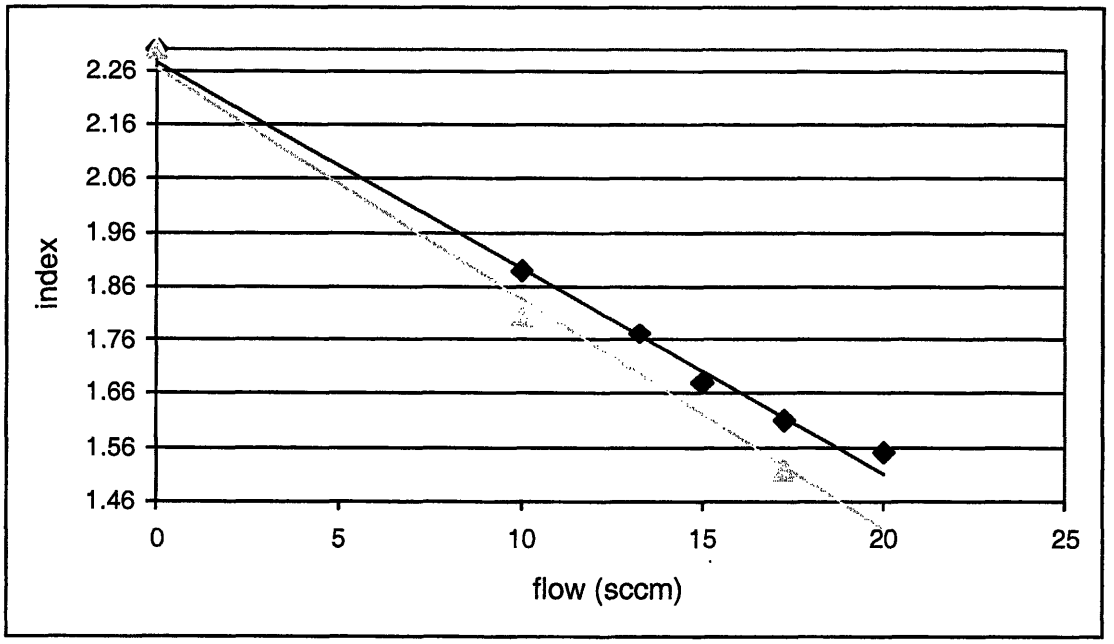

Figure 4.1: Theoretical prediction and experimental measurement of index vs. gas flow (10% O_2 in Ar) rate at 400W and 500W target power. ($\triangle$ = 400 W, $\Diamond$ = 500 W, solid lines are theory)

silicon rich. A linear combination of the refractive indices of Si and Si_3N_4 indicate that Si-rich Si_3N_4 alloys, as demonstrated, have an approximate composition of 18% Si in 82% stoichiometric Si_3N_4.

4.2.2 Film Roughness

The roughness of the sputtered SiON films were determined using Atomic Force Microscopy. A Digital Instruments Nanoscope IIIa Scanning Probe Microscope was used. Figure 4.2 shows the variation in RMS roughness with change in (10% O_2 in Ar) gas flow rate.

The increase in roughness as the gas flow rate increases can be attributed to the decrease in energy (and therefore surface mobility) as the depositing species arrive on the surface of the substrate. The energy decreases with increasing gas pressure because the depositing species make more collisions (and therefore lose more energy) at higher pressures.

Film roughness is an important parameter to minimize, because excessive film roughness can cause light scattering in waveguides, especially at higher index contrasts. In the case that the film roughness is high for a particular application, chemical-mechanical polishing (CMP) can be employed to reduce film roughness and minimize light scattering.

4.2.3 Film Stress

Film stress measurements were performed using a Tencor FLX 2320 Thin Film Stress Measurement system. The measured stresses are shown in Table 4.1.

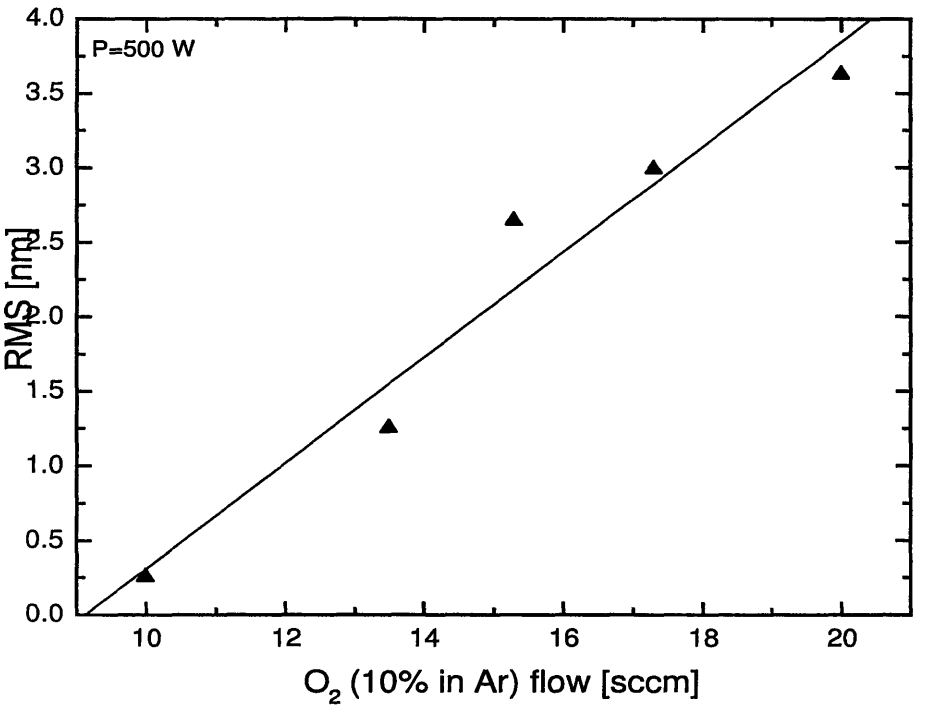

Figure 4.2: Variations in roughness vs. gas flow (10% O_2 in Ar) at 500 W. Values are RMS roughness, and are calculated from 1μm square scans.

Index	Ar/O_2 Flow	Stress
1.55	20 sccm	-70 MPa
1.61	17.3 sccm	-78 MPa
1.68	15 sccm	-76 MPa
1.89	10 sccm	-200 MPa
2.29	7 sccm (Ar only)	-410 MPa

Table 4.1: Stresses of sputtered silicon oxynitride films. All films were deposited at 500 W power, and the Ar/O_2 flow was varied in order to tune the refractive index of the film.

Table 4.1 shows that the film stress increases as the deposition pressure decreases. This increases is consistent with the decrease in film roughness that was observed when the flow rate was decreased. Both data indicate that the energy of the atoms arriving at the substrate is highest when the pressure in the reaction chamber is lowest. The stress data also demonstrate that all of the sputtered films are in compression. This compressive film stress is due to the impact of the highly energetic species onto the depositing film.

4.2.4 Composition Analysis

Compositional analysis was performed on thin silicon oxynitride films deposited on silicon substrates. The composition was determined from wavelength dispersive spectroscopy (WDS) using a JEOL JXA-733 Superprobe. The silicon, nitrogen, and oxygen compositions as determined by WDS are shown in Figure 4.3.

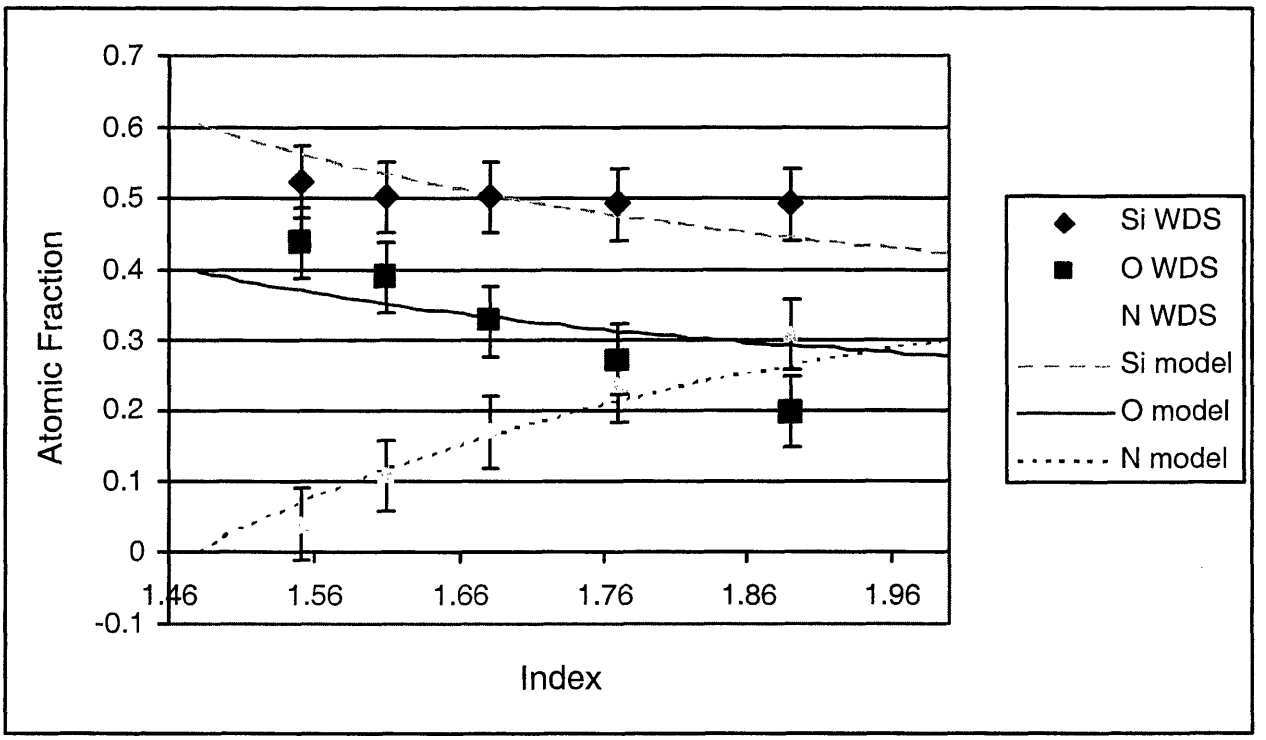

Figure 4.3: WDS compositional analysis of various SiON films. Both experimentally determined data and theoretically predicted data are shown.

It is important to note that the WDS compositional analysis may somewhat overestimate the amount of silicon (and underestimate the amount of nitrogen and oxygen) in the films. Because the SiON films are deposited on a silicon substrate, part of the silicon signal may come from the underlying silicon. However, since all of the films analyzed are on the order of 1μm, the majority of the signal comes from the sputtered films.

The theoretical compositions shown in Figure 4.3 is based on the reactive sputtering model given in Section 3.3.4. From this section, we can write the refractive index of reactively sputtered SiON as a linear combination of the refractive indicies of SiO_2 and of Si-rich Si_3N_4 (SiN):

$$n = f(n_{SiO_2}) + (1 - f)n_{SiN} \tag{4.1}$$

where $n_{SiO_2} = 1.46$ and $n_{SiN} = 2.3$. The relative amounts of silicon, oxygen, and nitrogen in the oxynitride can then be determined from the stoichiometric ratios of these elements in the oxide and nitride. The mole fractions of oxygen, nitrogen, and silicon ([O], [N], [Si]) can be written as follows:

$$[O] = \frac{2}{3}f \tag{4.2}$$

$$[N] = \frac{1}{2}(1 - f) \tag{4.3}$$

$$[Si] = \frac{1}{3}f + \frac{1}{2}(1 - f) \tag{4.4}$$

The WDS analysis shown in Figure 4.3 indicates that the atomic concentrations predicted by our model are in good agreement with the atomic concentrations measured using WDS. Furthermore, the Si concentrations determined by WDS show that the Si concentration in the sputtered films is much too high to be attributed to stoichiometric SiON.

4.2.5 Morphology

Figure 4.4 shows a transmission electron microscopy cross section of a reactively sputtered SiON film (n=1.89). This micrograph shows that the sputtered SiON film is very uniform, with no visble grains, columnar structures, or voids. Additionally, in order to ensure that the sputtered films are fully consoladated, annealing studies were performed on silicon nitride films (n=2.3). Details of these annealing studies are given in Section 5.3. This annealing shows that the index and the thickness of these Si_3N_4 films change less then 1% after a two hour high temperature anneal. This small change in film properties indicates that the as-deposited sputtered films are nearly fully dense.

4.2.6 Bond Analysis

Fourier Transform Infrared Spectroscopy

Fourier Transform Infrared Spectroscopy can provide a variety of information about the bonding within silicon oxynitride films. A variety of prominent features are visible in the mid-IR spectrum for both silicon dioxide and silicon nitride. SiO_2 demonstrates absorption bands at 1075, 800, and 450 cm^{-1}, which correspond to the stretching, bending, an rocking vibrations of the SiO_2 [54]. Of these bands, the stretching vibration at 1075 cm^{-1} is

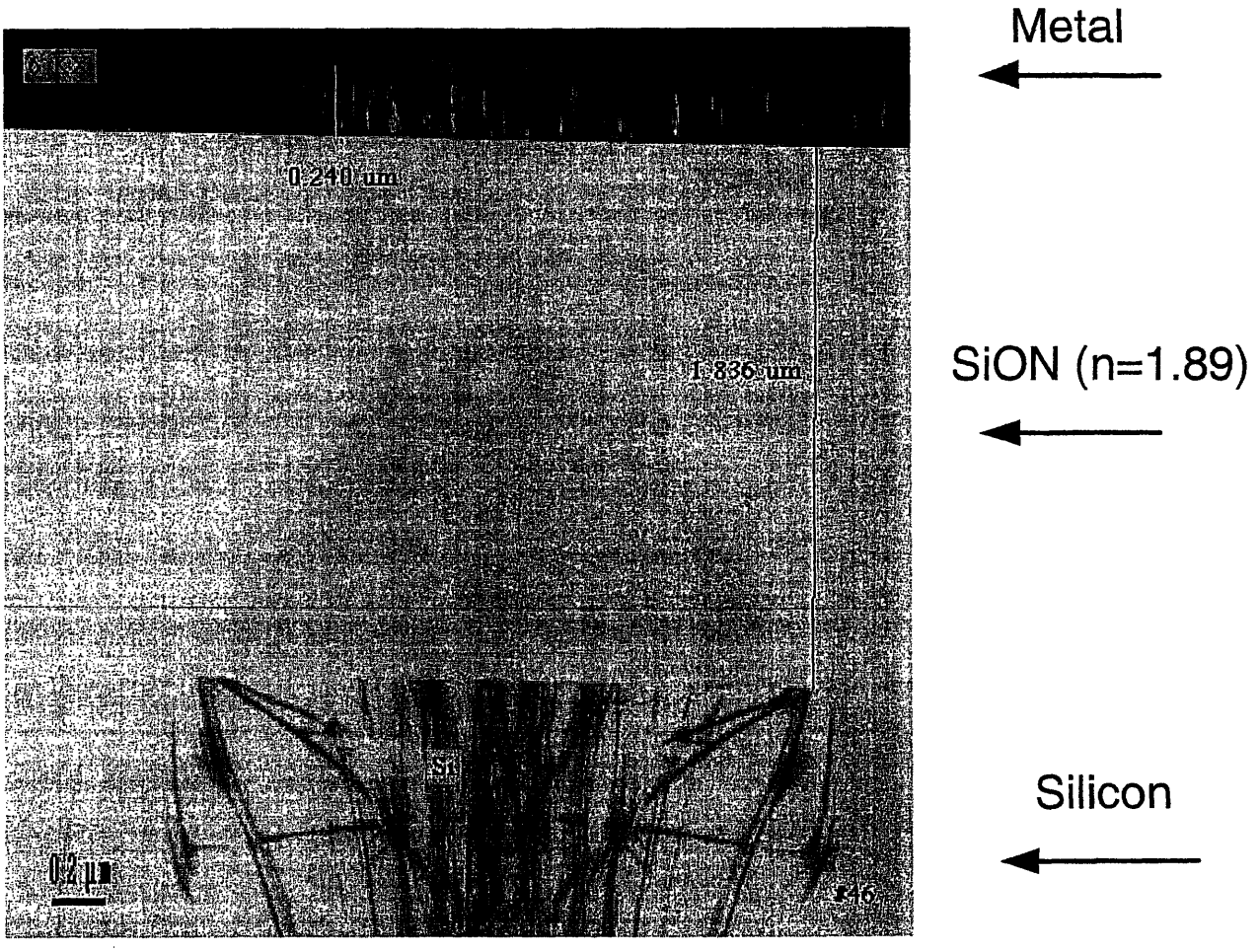

Figure 4.4: TEM cross section of reactively sputtered SiON (n=1.89).

the most prominent feature [55]. Additionally, silicon nitride exhibits a strong stretching absorption band between 830 cm^{-1} and 890 cm^{-1} [55]. The hydrogen content of a film can also be determined from the FTIR spectrum. N-H has a stretching frequency at 3350 cm^{-1}, and Si-H exhibits a stretching frequency at 2160 $^{-1}$ [56].

Figure 4.5 shows the variation of the main spectral feature as the composition of the SiON film moves from being oxide-rich to being nitride rich. As this figure shows, the Si-N feature and the Si-O feature are not realized as two separate features, but instead as one overlapping Si-(O, N) absorption band [57]

Figure 4.6 shows the variation of the location of this Si-(O,N) spectral feature with index. Literature values for silicon nitride and silicon dioxide are also shown in this figure. Numerous authors report a continuous variation of the position of the Si-(O,N) peak with index [58] [59] [60] [98]. The smooth, linear shift in peak position shown in 4.6 can be taken as an indication that the films are forming a homogeneous alloy of silicon nitride and silicon dioxide [60]. Figure 4.6 shows that the FTIR peak positions for the sputtered films lie above the theoretically predicted line. This deviation is taken as an indication that the sputtered SiON films are silicon rich, because additional silicon in the film would raise the refractive index of a film for a given SiO_2/Si_3N_4 ratio. This silicon-rich behavior is consistent with both the refractive index data and the WDS data presented in previous sections. Si-rich RF-sputtered silicon nitride deposited under similar processing conditions (from an Si_3N_4 target in an Ar plasma) has also been reported in the literature [61] [62].

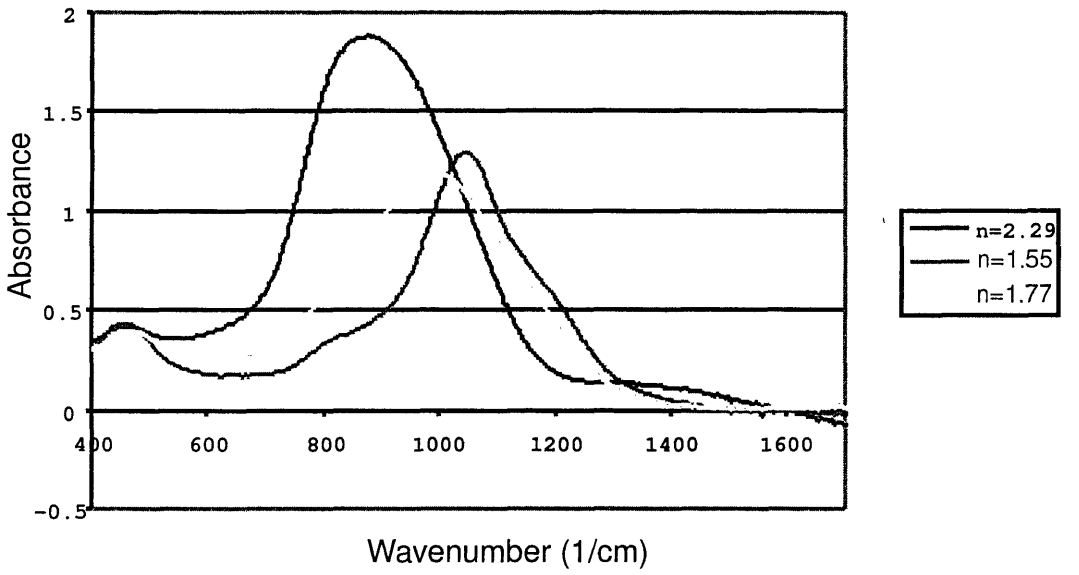

Figure 4.5: The variation of the main FTIR Si-(O,N) absorption band in SiON and Si_3N_4 of various compositions. Films were sputtered at 500 W.

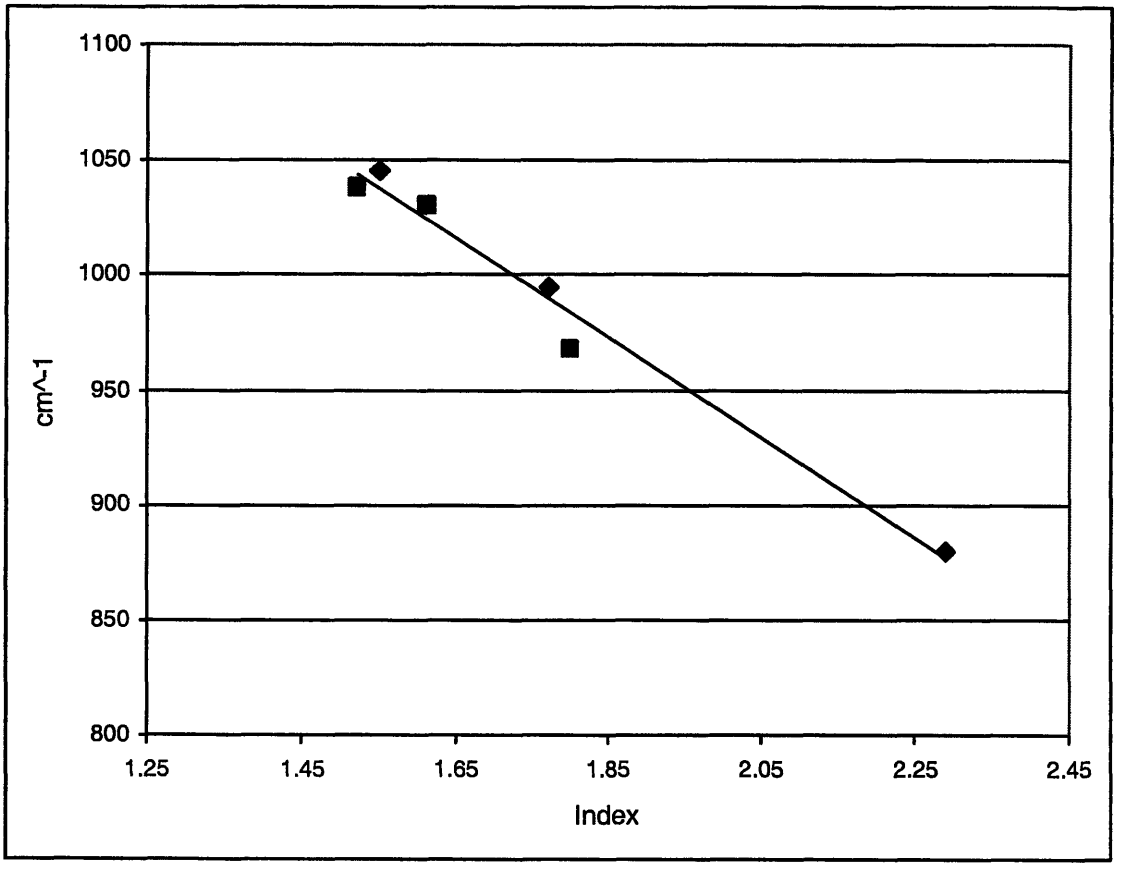

Figure 4.6: Variation of Si-(O,N) peak position with index. △ are experimental points at 400 W. ◊ are experimental points at 500 W.

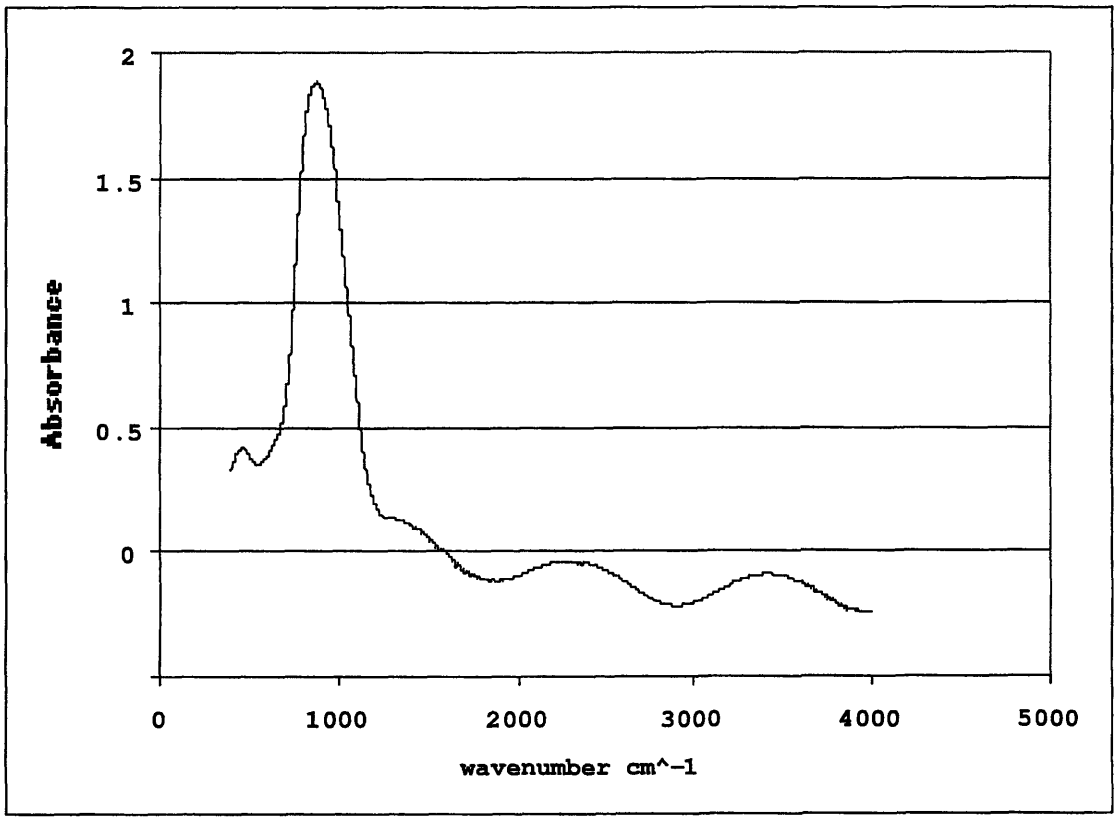

Figure 4.7: FTIR spectrum of sputtered silicon nitride film (500 W).

Figure 4.7 shows a full FTIR spectrum for sputtered Si_3N_4. No N-H (3350 cm^{-1}) or Si-H (2160 cm^{-1}) peaks are resolvable in this spectrum. (The regularly varying features in this feature are not absorption bands; these features are caused by interference effects due to the film thickness.) In contrast, Bona et al. report hydrogen contents of 16% in their PECVD deposited SiON films [63].

4.2.7 Raman Spectroscopy

Raman Spectroscopy was performed on films deposited under a variety of different deposition conditions. Raman analysis was performed using a Kaiser Hololab 5000R Raman Spectrometer. The wavelength used was 514.5 nm. The spot size was 100 μm^2. No polarizer was employed during measurement. All samples were deposited onto a glassy carbon substrate in order to prevent the substrate signal from interfering with the film measurements.

Figure 4.8 shows the Raman spectra of sputtered silicon oxynitride and silicon nitride deposited under a variety of conditions. The broad peak located from 800-1100 cm^{-1} is attributed to Si-N bonds [66] [67] [68] [69]. Lin et al. attribute this broad feature to two peaks, one present at 870 cm^{-1} and the other present at 1080 cm^{-1} [70]. A transverse optical mode of amorphous silicon is commonly reported around 480 cm^{-1} [71] [72] [73]. This amorphous TO Si mode has been observed in sub substoichiometric Si_3N_4 [68] [67]. Peaks at 1340 cm^{-1} and 1590^{-1} are due to the glassy carbon substrate [74].

Figure 4.8 shows that the Si-Si peak that is prominent in all of the silicon nitride samples disappears in the reactive sputtered and co-sputtered nitrides. This Raman result is consistent with the analysis presented in the previous section. In the this section, we showed that during the reactive sputter process the oxygen reacts with the free silicon to produce silicon oxynitride. This oxygen reaction serves to explain the disappearance of the Si-Si peak from the reactive sputtered Raman spectrum. Additionally, we showed that

co-sputtering serves to getter additional nitrogen into the deposited sample. This nitrogen gettering is confirmed by the lack of Si-Si signal in the co-sputtered sample.

4.3 Conclusions

This chapter has demonstrated that sputtered silicon oxynitride has the materials properties needed to make a good microphotonic waveguide material. The refractive index is shown to be easily tuned by varying either the target power or rate of reactive gas flow into the deposition chamber. This index can also be easily predicted by the model presented in Chapter 3; WDS measurements and Raman analysis have both shown that the composition of these films is also consistent with this model. The stress and film roughness have been both demonstrated to be low to moderate in all films. FTIR analysis reveals no presence of hydrogen in silicon nitride films, and shows the reactively sputtered SiON films to be a homogeneous alloy. In conclusion, materials analysis has shown sputtered SiON to have numerous properties desired in a microphotonic waveguide material.

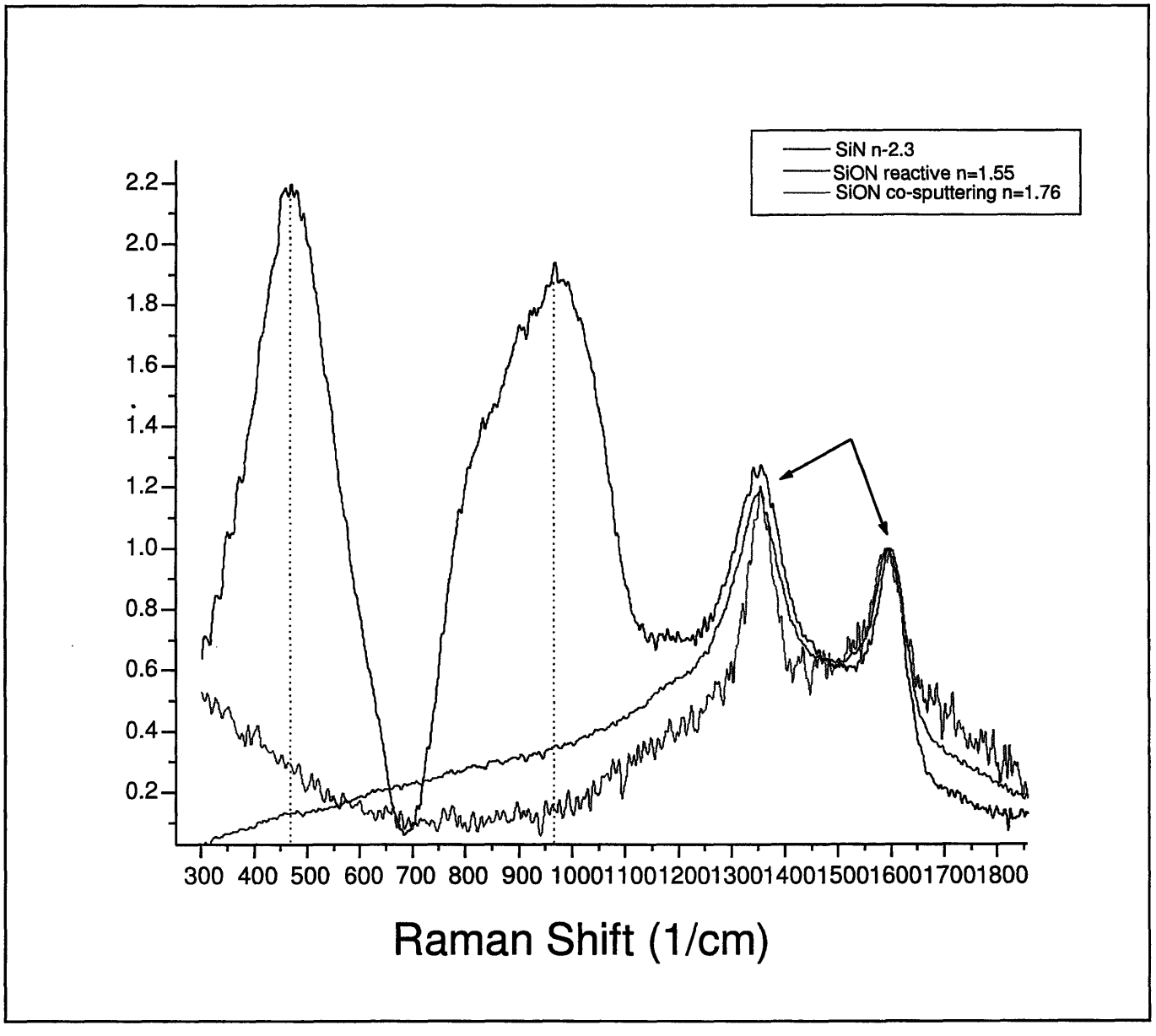

Figure 4.8: Raman spectra of sputtered Si_3N_4, reactively sputtered SiON, and cosputtered SiON

Chapter 5

Waveguide Loss Measurements

This chapter presents waveguide loss measurements of waveguides that have sputtered SiON or sputtered Si_3N_4 as a core material. First, an overview of the prism coupling method of loss measurement is presented. A specific methodology for making prism coupling measurements is given, and slab waveguide loss measurements are presented. Finally, sputtered Si_3N_4 channel waveguides are demonstrated.

5.1 Prism Coupling Measurements

Prism coupling provides a easy and accurate way to determine the index (n) and thickness (t) of a thin film. Prism coupling can also be used to determine the loss in slab waveguides.

5.1.1 Index and Thickness Measurements

Figure 5.1 shows a basic prism coupling setup. The prism coupling method works by shining a laser beam into a prism. The prism is kept in intimate contact with the film by a mechanical plunger that presses against the film. The prism, along with a detector, are mounted onto a rotary table which scans through a range of angles; the laser beam always enters from a fixed direction. At the majority of angles, there is no coupling between the prism and the film, and all of the light is reflected into the detector. However, at certain angles, the phase velocity of the light in the prism in the direction parallel to the film will match the phase velocity of one of the characteristic modes of propagation within the slab waveguide [14]. When these two phase velocities are equal, light couples from the prism into the film, and the detector shows a sharp dip in light intensity. These mode angles, being characteristic of film thickness and index, are then used to calculate the properties of the thin film.

There are a number of advantages that prism coupling has over other index measurement methods, such as ellipsometry. First, the calculation of n and t depends only on the coupling angle; therefore, film properties such as absorption do not influence the calculation. (Films with losses as great as 80 dB/cm can be accurately measured using prism coupling [14]). Furthermore, if more than two modes are found, each set of modes can be used to calculate n and t, verifying the accuracy of the measurement. One disadvantage of the prism coupling method is that the film must be thick enough to support two modes in order to measure n and t simultaneously. (This thickness is on the order of $0.5\mu m$, and depends on the index

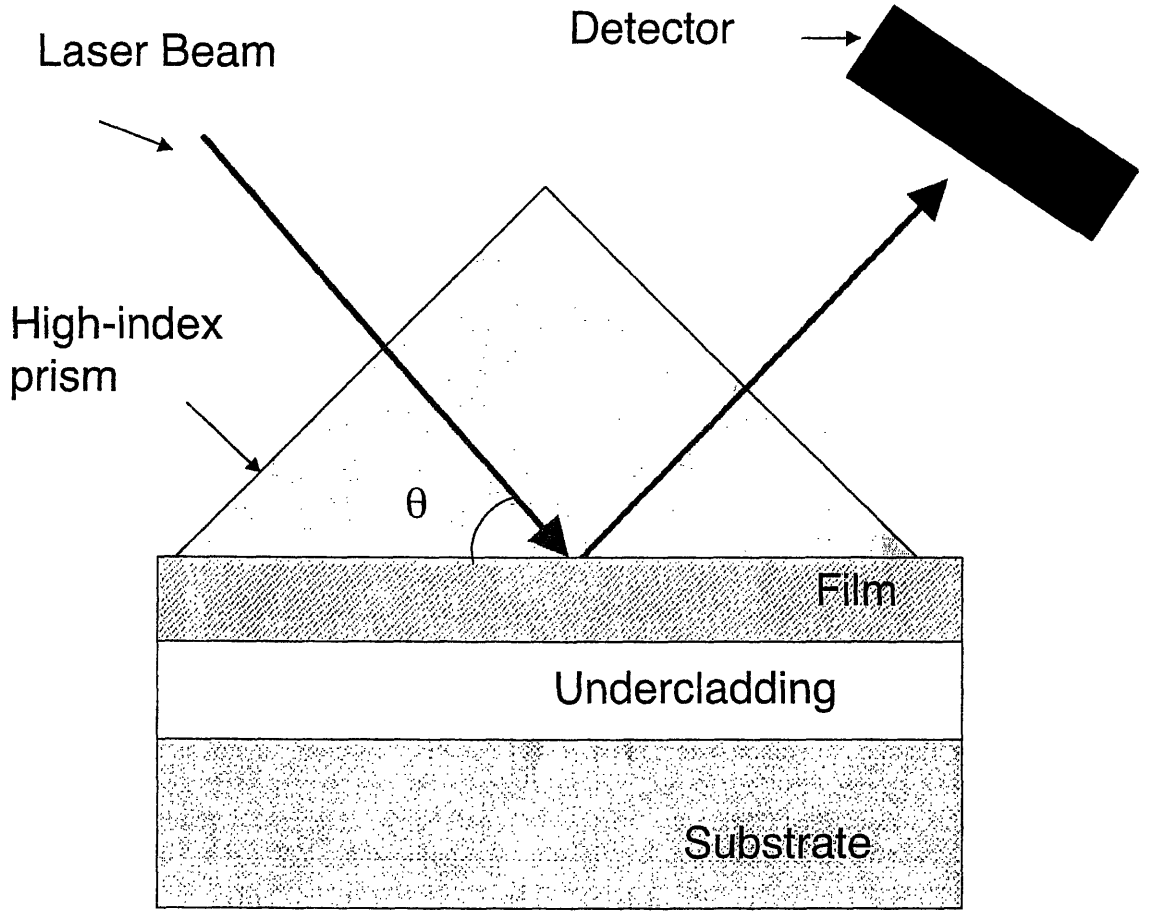

Figure 5.1: Prism coupling setup [19]

of the film.) However, if one variable is known, the other can be calculated from a single mode.

5.1.2 Slab Loss Measurements

Prism coupling can also be employed to measure the losses in unclad slab waveguides. Figure 5.2 shows a basic loss measurement setup. All prism coupling loss measurements were made using a Metricon Series 2010 prism coupler with loss measurement attachment.

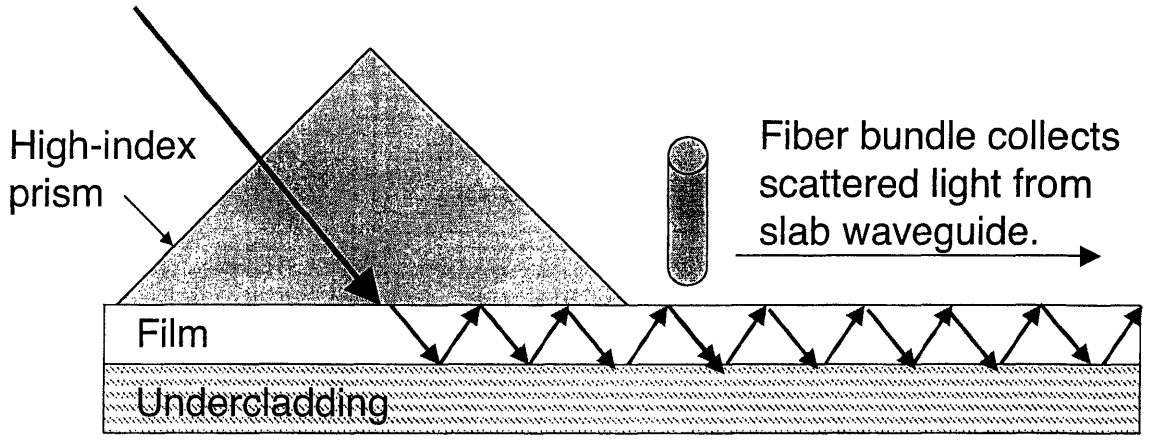

Figure 5.2: Loss measurements using Metricon 2010 prism coupler

In order to measure losses, light is first coupled into a slab waveguide using the prism. The rotary table is left at a coupling angle, and a fiber is scanned down the length of the waveguide. Light scattered out of the waveguide (which is proportional to the light propagating within the waveguide) is measured. Knowing the rate of light decay in the waveguide, the waveguide loss can be calculated.

Detailed Loss Measurement Description

In order to provide the most accurate loss measurements using the Metricon prism coupling setup, the following procedure was followed. First, an angular scan was performed on the waveguide in question. The mode of interest was selected, and the position of the laser beam was adjusted in order to maximize the amount of light coupling into the film. (This laser beam adjustment is especially important when using a longer wavelength laser beam. Overcoupling into the film can be a problem at these longer wavelengths, and the laser beam must be slightly mis-aligned in order to provide the best film coupling [107].) The

rotary table is then rotated to the position of maximum film coupling.

The fiber bundle is then moved into place to measure the propagating light. The gain of the fiber's detector is reduced to a minimum in order to maximize the signal to noise ratio. If the signal is too strong, the beam is attenuated until the signal is on scale. A loss shield is placed between the prism and the fiber bundle in order to reduce the amount of scattered light reaching the fiber. The fiber is then scanned along the length of the waveguide.

Before a loss can be calculated from this scan, it is very important to confirm that the majority of the light detected by the fiber is in fact coming from the guided light within the waveguide. In particular, it is important realize that when the fiber is close to the prism, some of the light detected may actually be light scattered from the prism. Conversely, signal observed at the end of a scan may simply be detector noise and not guided light.

The source of the light at any fiber position can be determined by performing an angular scan at that location. Rotating the rotary table about the mode position should produce a sharp peak in intensity at the coupling position. If the background signal is high on either side of the mode position, we can conclude that there is a great deal of light being scattered into the detector from the prism. If no peak is observed, we conclude that the signal observed is only noise and not related to the guided light. Ideally, the loss measurement should be restricted to the length where there is a sharp peak at the coupling angle, and little or no signal on either side of the coupling position. This segment is selected for loss

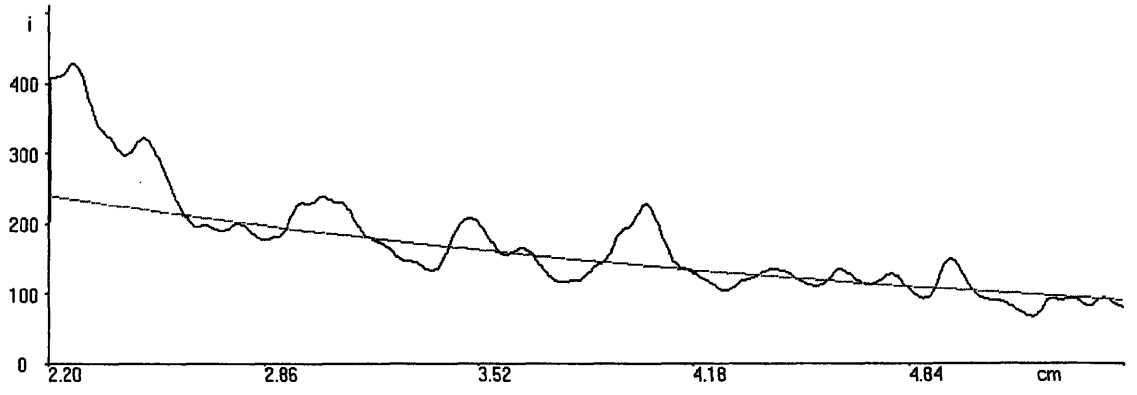

Figure 5.3: Loss measurement of silicon oxynitride film (n=1.55) on oxide using Metricon prism coupler

measurement. Again, a fiber scan is performed, and an exponential decay is fit to the drop in intensity. The slab loss is calculated from this exponential fit.

Uneven Surface Scattering

Loss measurements using the Metricon prism coupling setup are most easily and accurately accomplished when the light scattering from the top of the guiding film is uniform. However, due to inhomogeneities in the sputtered silicon oxynitride films, there is some non-uniform scattering from the guiding layer. Figure 5.3 shows a typical loss profile from a low loss silicon oxynitride layer.

The importance of the error introduced from this surface scattering is dependent on the loss in the guiding film. A simple simulation was performed to determine the error introduced by scattering loss as a function of film absorption. This calculation is described below.

Surface Scattering Calculations

In order to determine the importance of surface scattering centers, the following analysis was performed. The intensity of the light in the slab waveguide were first plotted as $I(x) = I_0 e^{-\alpha x}$. Simulated scattering centers were then placed at regular intervals. These scattering centers were assumed to scatter four times as much light as the regular waveguide material. A best-fit exponential was then fit to the intensity as a function of distance. The change in calculated absorption coefficient produced from the scattering centers and the percentage change in absorption coefficient are plotted in Figure 5.4. This figure demonstrates that the absolute error introduced by surface scattering increases as the absorption of the film increases. The percentage error ($\Delta(\alpha)/\alpha$), however, is worst in low loss slabs.

5.2 Slab Waveguide Loss Measurements

5.2.1 Sample Preparation

SiON and Si_3N_4 thin films were deposited onto 3 μm of thermal oxide on silicon. (There are a few exceptions. Samples #1, #4, and #7 were deposited onto 15 μm thermal oxide.) All of the guiding layers were between 1 and 2 μm thick. In order to reduce the roughness, some films underwent chemical-mechanical polishing (CMP) after deposition (Table = 25 RPM, Quill = 40 RPM, Down force = 3 psi, Slurry=150 ml/min, Back force = 2psi, Polishing time = 150 sec.) In each case the primary mode was measured. Measurements were made using TE polarized 1554 nm light. All films are unannealed.

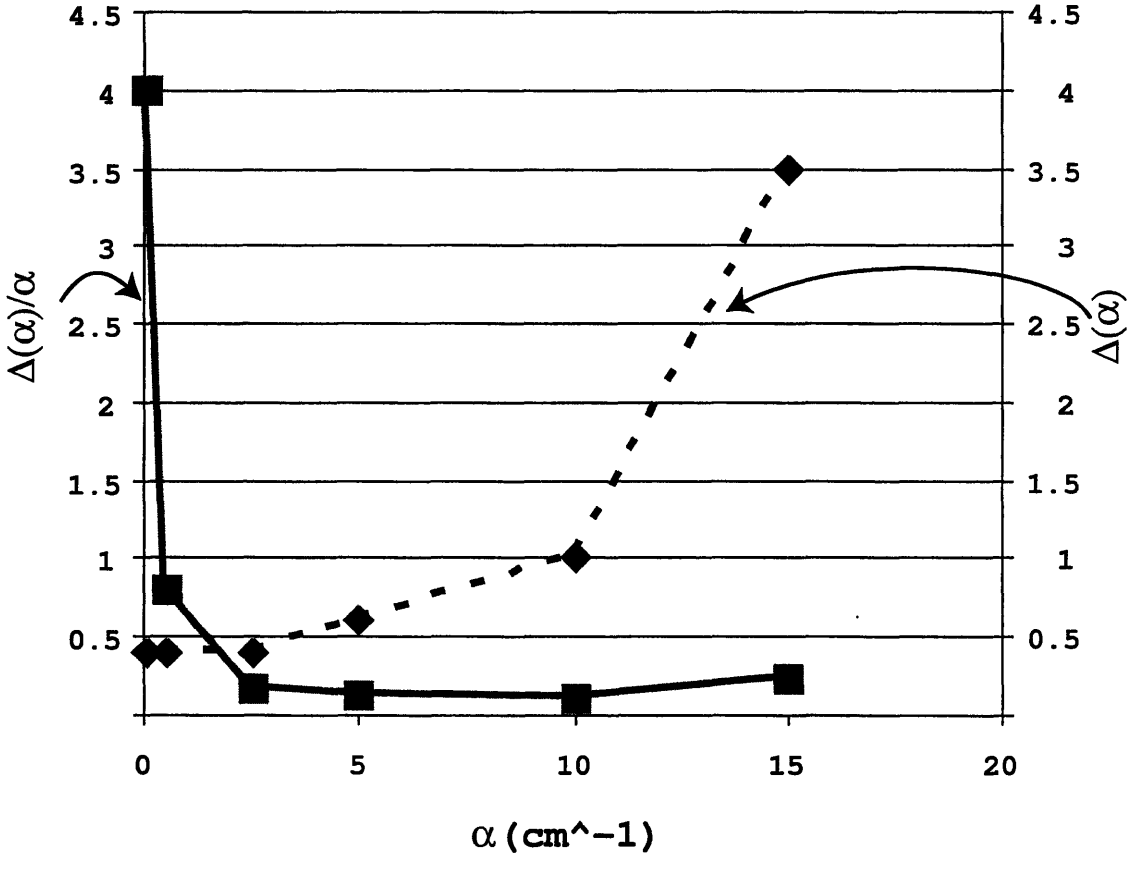

Figure 5.4: Error in loss (α) and fractional error in loss ($\Delta(\alpha)/\alpha$) caused by the introduction of scattering centers in simulated slabs.

Sample	Index	Flow	Power	CMP?	Loss
#1	1.61	17.3 sccm Ar+ O_2	500 W	No	10 dB/cm
#2	1.52	17.3 sccm Ar + O_2	400 W	No	1.5 dB/cm
#3	1.55	17.3 sccm Ar + O_2	400 W	Yes	1.2 dB/cm
#4	1.89	10.0 sccm Ar + O_2	500 W	No	6 dB/cm
#5	1.8	10.0 sccm Ar + O_2	400 W	No	4 dB/cm
#6	1.8	10.0 sccm Ar + O_2	400 W	Yes	1.8 dB/cm
#7	2.3	7.0 sccm Ar	500 W	No	> 15 dB/cm
#8	2.3	7.0 sccm Ar	400 W	No	> 15 dB/cm
#9	1.65	7.0 sccm Ar	400 W SiO_2 200 W Si_3N_4	No	0.7 dB/cm

Table 5.1: Slab Waveguide losses of various unannealed films at 1554nm. Waveguides have an SiO_2 undercladding (n=1.46) and an air overcladding (n=1).

5.2.2 Waveguide Losses

Table 5.1 shows the losses of a variety of slab waveguides prepared under various processing conditions.

The data in Table 5.1 demonstrates that the highest waveguide losses are observed in the sputtered silicon nitride sample. Table 5.1 also demonstrates that decreasing the power applied to the target decreases the loss in the film. Index measurements have revealed that decreasing the power to the target increases the amount of oxygen gettered into the depositing film (as evidenced by the decrease in refractive index.) We can deduce that this

extra oxygen satisfies some of the unbonded silicon that we know arrives at the surface of the substrate from the nitride target. This oxygen incorporation may improve the quality of the sputtered film, therefore reducing the loss in the waveguide. The best loss is achieved by the cosputtered silicon oxynitride film, where is no liberated nitrogen observed by the RGA.

5.2.3 Film Roughness and Waveguide Losses

Losses in slab waveguides can come from both intrinsic materials properties and from extrinsic factors, such as scattering losses due to film roughness (See Figure 5.5). Intrinsic materials losses can be caused by multiple factors including bond vibrations (such as N-H bond absorption), dangling bond absorption, and film non-uniformities. In order to fully analyze the sources of intrinsic materials loss in the guiding films, we must first understand the loss introduced from light scattering due to waveguide roughness.

Surface scattering is one of the main sources of non-absorption related losses in optical waveguides. In order to determine the extent of the scattering loss in the sputtered SiON slab waveguides, simulations were performed. Rsoft's BeamPROP beam propagation method simulator was used to perform the simulations. Slab waveguide structures with thicknesses and indices given in Table 5.2 were used. These waveguide parameters correspond to those of the waveguides whose optical losses were measured using prism coupling. The difference between the measured loss and the simulated loss (Δloss) is also shown in Table 5.2. The parameter Δloss is taken to be the loss introduced from intrinsic materials

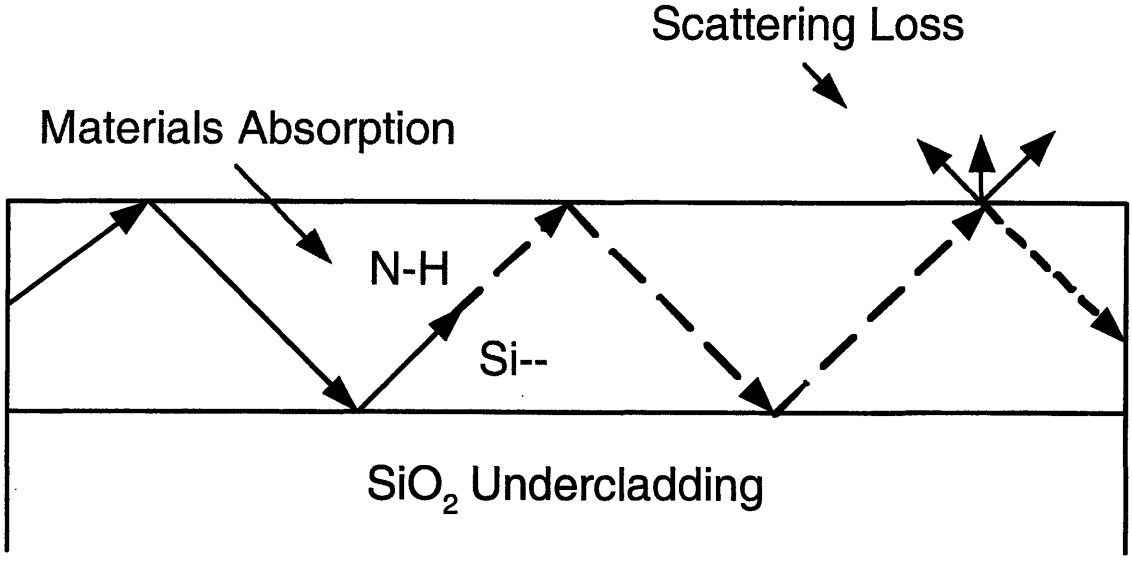

Figure 5.5: Sources of waveguide loss. Intrinsic losses arise from materials specific sources, such as dangling bonds, vibrational absorption, and film non-uniformity. Extrinsic scattering losses become more significant as roughness increases and as index contrast increases.

Index	Thickness	RMS Roughness	CMP ?	Exp. Loss	Calc. Loss	ΔLoss
1.50	1.84 μm	93 A	No	1.5 dB/cm	0.22 dB/cm	1.28 dB/cm
1.54	1.96 μm	47 A	Yes	1.2 dB/cm	0.04 dB/cm	1.16 dB/cm
1.8	1.7 μm	110 A	No	4 dB/cm	1.3 dB/cm	2.7 dB/cm
1.80	1.71 *mum*	47 A	Yes	1.8 dB/cm	0.2 dB/cm	1.6 dB/cm
2.3	0.6 *mum*	37 A	No	18 dB/cm	5.0 dB/cm	13 dB/cm

Table 5.2: Slab Waveguide Properties. Losses are given at 1554 nm.

sources.

Table 5.2 demonstrates a few characteristics of scattering loss due to roughness. First, the scattering losses increase as the index contrast increases. Second, the losses improve when CMP was used to reduce the surface roughness. The RMS roughness numbers shown in Table 5.2 are not the AFM values discussed in Section 3. Though the short-scale (1 μm) roughness of the sputtered SiON samples is quite low, the short-scale roughness does not completely describe the surface roughness of these samples. Because these sputtered SOiN samples exhibit a longer-scale roughness as well, profilometry was used to determine the roughness of the sputtered samples over several hundred microns. Measurements were made using a Tencor P-10 Surface Profilometer.

Clearly, film roughness contributes to the waveguide losses measured. In particular, scattering losses are shown to be a large proportion of all of the losses observed in the lower-loss slab waveguides. However, especially at higher index contrasts, surface scattering cannot

explain the entirety of the losses measured in these waveguides.

One of the most likely sources of intrinsic materials loss is loss due to silicon dangling bond absorption. In Chapter 3, we determined that the sputtering silicon nitride does not deposit stoichiometrically (as Si_3N_4). Instead, the nitride has a composition close to that of SiN. If the excess silicon incorporates substitutionally, this means that instead of each Si being bonded to 1.25 N atoms, each Si is bonded to only 1 N atom, resulting in one dangling bond for every 3 Si atoms in the sub-stoichiometric silicon nitride.

Likewise, as shown in Chapter 3, the reactively sputtered SiON films are expected to maintain some of the silicon-rich characteristics of the SiN films. Taking the index of the SiON films to be a linear combination of SiN and SiO_2, we find that for n = 1.8, the film is 40% SiN, and for n = 1.55, the film is 11 % SiN. This corresponds to 1 dangling bond for every 7.5 Si, and 1 dangling bond for every 27 Si, respectively.

Figure 5.6 shows a plot of the excess slab waveguide loss vs. the percentage of Si atoms in the film which have dangling bonds associated with them. (The excess slab waveguide loss is defined as the loss not accounted for by scattering losses.) The calculated points are calculated assuming that all of the loss observed in the n = 1.5 waveguides is caused by dangling bond absorption. This figure demonstrates that, though we do not get a perfect fit, there is a strong correlation between an increase in loss and an increase in silicon dangling bonds. Thus, we can attribute the losses observed in the slab waveguides

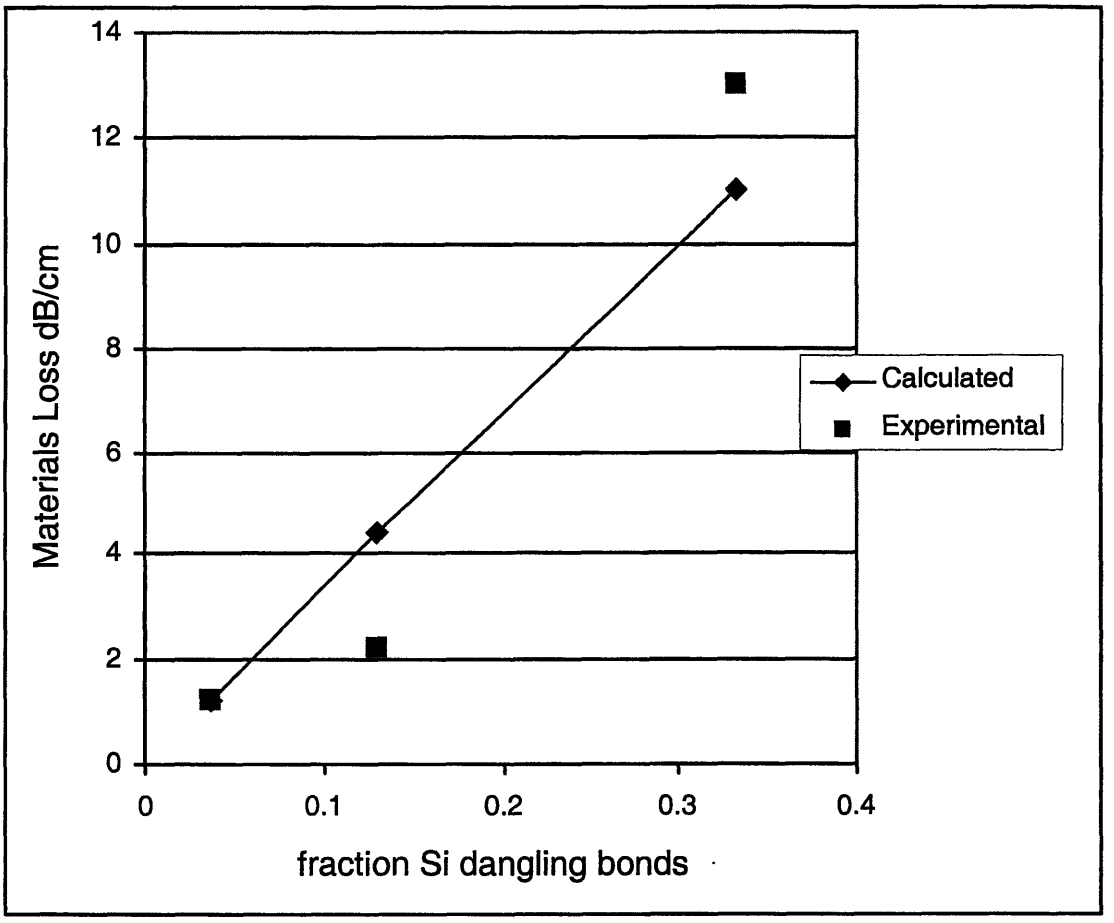

Figure 5.6: Materials slab waveguide loss vs. % of silicon dangling bonds.

to losses arising from both scattering loss and dangling bond absorption. The lowest losses are predicted and observed in the cases where film roughness and excess silicon can be kept to a minimum.

5.3 Sputtered Silicon Nitride Channel Waveguides

This section examines the losses of single mode channel Si_3N_4 waveguides. The losses of annealed and unannealed waveguides are constrasted.

5.3.1 Waveguide Processing

Silicon nitride films are deposited onto 3 μm of thermal oxide. Films are sputtered from a Si_3N_4 target. The flow rate of Ar into the sputtering chamber is 7 sccm, and the target power is 500W. Deposition is performed at room temperature, and the pressure in the chamber during deposition was $3.7x10^{-4}$ torr. The film thickness is 0.3 μm. Waveguides are fabricated from both unannealed films and films that were annealed at 1050°C for 2 hours in an N_2 ambient.

Straight 1 μm wide waveguide segments are patterned on the Si_3N_4 film using a Nikon i-line stepper. The waveguides are etched using an Applied Materials AME 5300 under the following conditions: the etching gas is C_2F_6 (30 sccm), the source RF bias is 1650 W, and the wafer bias is 450W. A 3μm SiO_2 overcladding is deposited using a Novellus Concept 1 PECVD. A schematic of these channel waveguide structures are shown in Figure 5.7.

5.3.2 Channel Waveguide Measurements

After fabrication, the wafers are diced, and the waveguide facets are polished using a Buehler ECOMET 3 in order to facilitate fiber-to-waveguide coupling. Waveguide loss is

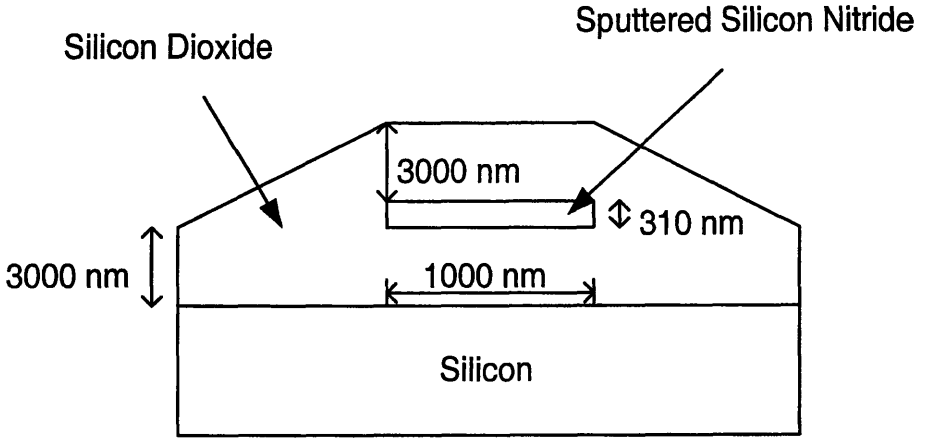

Figure 5.7: Schematic of sputtered nitride channel waveguide

measured using the Fabry-Perot resonance method. Loss is calculated using the following equation:

$$\alpha = -\frac{1}{L}\frac{1}{R} ln \frac{\sqrt{I_{max}/I_{min}} + 1}{\sqrt{I_{max}/I_{min}} - 1} \tag{5.1}$$

where L is the length of the waveguide, I_{max} is the maximum intensity of the resonance, I_{min} is the minimum resonance intensity, and R is the reflectivity as calculated using the FDTD method. Losses are measured at 1550nm.

The thickness and refractive index of the pre- and post-anneal films are shown in Table 5.3. Table 5.3 shows that there is very little film consolidation upon high-temperature anneal. The film only shrinks 0.97 % after a two hour anneal, and the refractive index (at 1550 nm) increases 0.23 %. This small change in refractive index and thickness indicates that the films are almost fully consolidated after deposition.

Sample	n(633nm)	n(1550nm)	thickness μm
unannelaed	2.191	2.182	0.310
annealed	2.221	2.187	0.307

Table 5.3: Index and thickness of films used in channel waveguides.

Sample	Loss (dB/cm)	Transmission(%/cm)
unannelaed	> 40	<0.01
annealed	19.4 +/- 10	1.161 +/- 1.5

Table 5.4: Losses in Sputtered Silicon Nitride Channel Waveguides. Courtesy of Dr. Shoji Akiyama

The waveguide losses are shown in Table 5.4. The losses in the unannealed silicon oxynitride waveguides are quite high, over 40 dB/cm. The waveguide materials improve upon annealing, and the losses in the annealed waveguides drop to 19 dB/cm.

Table 5.4 shows a result that is consistent with the slab waveguide loss measurements presented in the previous section, which showed that the sputtered silicon nitride films had much higher losses than films prepared by either the reactively sputtered or the co-sputtered methods. As discussed previously, the RGA analysis demonstrating liberated nitrogen in the reaction chamber indicates that the sputtered silicon nitride films will be of poorer quality than the reactive and co-sputtered films.

Improvements in channel waveguide performance would be expected if the guiding layer was changed from sputtered Si_3N_4 to either a guiding layer of co-sputtered SiON or a layer of reactively sputtered SiON. Table ?? demonstrates the processing conditions that produce the lowest loss slab waveguides. These low-loss films should provide a significant improvement to the loss in these sputtered channel waveguides.

5.4 Conclusions

In this chapter, we have demonstrated waveguides utilizing most of the range of indices available in the silicon oxynitride materials systems. As-deposited waveguides have been realized with losses below 1 dB/cm. These losses are an order of magnitude lower than those reported from as-deposited PECVD processing [116]. Losses below 2 dB/cm have been demonstrated for high index SiON waveguides (n=1.89); these high indices are particularly difficult to achieve using traditional PECVD processing. The higher losses that are demonstrated under certain processing conditions are shown to correlate with the high Si-dangling bond concentration predicted by the sputter model presented in Chapter 3.

Chapter 6

Active Device Applications of Sputtered SiON

Chapters 2, 3, and 4 demonstrated that high-quality, low-loss silicon oxynitride thin films for waveguide applications can be produced using a well-controlled sputtering process. However, the applications of sputtered silicon oxynitride and silicon nitride are not limited to passive waveguiding structures. Because film stoichiometry can be easily controlled using a sputter process, and because dopants can easily be incorporated into sputtered films, sputtered silicon oxynitride is an ideal candidate for producing novel materials for both passive and active optical devices. This section studies the use of sputtered SiON as a host material for erbium atoms. These Er-doped materials are studied for their potential use in Er-doped waveguide amplifiers.

6.1 Er-Doped Silicon Oxynitride

Sputter processing provides an easy method for doping materials without having to worry about the difficulties of carrier gasses or ion implantation. This section considered sputtered SiON as a host for erbium ions for use in Er-doped waveguide amplifiers.

6.1.1 Overview of Er-doped Amplifiers

Erbium-doped fiber amplifiers (EDFAs) are a critical component of fiber optic telecommunications systems. Er-doped amplifiers provide the light amplification that is necessary to make long-haul fiber optic communication possible. These optically pumped amplifiers exploit the three-level energy system within the erbium atom in order to create stimulated emmission in the device. This light amplification takes place in the 1.55 μm wavelength range, making it perfect for operations at telcom wavelengths.

The utility of EDFAs in telecommunications has prompted research into the development of Er-doped waveguide amplifiers for use in microphotonics networks. To date, most of this research has focused on Er-doped silica glass waveguides. As discussed previously, the use of silica waveguides has one unvoidable problem – large device footprint. Erbium-doped silicon nitride and silicon oxynitride provide a potential solution to this problem; their larger refractive indices allow for smaller bending radii and smaller devices. Additionally, silicon nitride has a larger erbium solubility than does silicon dioxide. These charactaristics make Si_3N_4 and SiON ideal candidates for investigation for use in waveguide amplifiers.

Saini et al. declare that two requirements must be met for a material to provide efficient light amplification to realize net gain [117]. The first is that the material must have low materials loss and low surface roughness (in order to minimize scattering losses). The second requirement is that the material have long spontaneous emission lifetime at room temperature, permitting population inversion at low pump powers. We have already demonstrated that sputtered SiON waveguides can be realized with losses below 1 dB/cm. This section explores the potential of realizing a long spontaneous emission lifetime in Er-doped sputtered SiON.

6.1.2 Processing of Er-Doped Material

Er-doped SiO_2, Si_3N_4 and SiON were produced using sputter, co-sputter, and reactive sputter processes similar to those used to produce the waveguides demonstrated in Chapter 5. Er-doping was accomplished by low power co-sputtering from an erbium target. Processing details are given in Figure 6.1. After deposition, films are annealed for 1 hour at 1000^o C in order to activate the Er atoms.

6.1.3 Lifetime Measurements

Photoluminescence intensity and lifetime measurements were made at room temperature and at 4K using an Oxford Instruments liquid helium cooled cryostat, using a mechanically chopped Ar-ion 488 nm laser as the excitation source. PL intensity was collected using a Spex spectrometer and liquid nitrogen-cooled Hamamatsu photomultiplier tube. Table 6.2 gives the lifetime measurements of the various annealed Er-doped samples.

Sample	SiO_2:Er	SiON:Er (react.)	SiON:Er (co-sp.)	Si_3N_4:Er
Ar gas flow (sccm)	7.1	–	7.1	7.1
Ar/O_2 gas flow (sccm)	–	13.1	–	–
SiO_2 Target Power	400 W	–	400 W	–
Si_3N_4 Target Power	–	400 W	200 W	400 W
Er target power		30 W	14 W	11 W
Refractive index (1554 nm)	1.457 (@633)	1.65	1.64	2.2
[Er] (cm^{-3})	$0.92x10^{20}$	$5.83x10^{20}$	$6.1x10^{20}$	$4.95x10^{20}$

Table 6.1: Deposition parameters of Er-doped samples.

	τ_{4K} (ms)	τ_{RT} (ms)	$\eta = \tau_{RT}/\tau_{4K}$
CVD SiO_2:Er	27	19	0.7
SiO_2	16.6	14	0.84
SiON:Er (react.)	5.24	0.48	0.09
SiON:Er (co-sp.)	10.62	3.8	0.36
Si_3N_4	2.4	0.487	0.2

Table 6.2: Lifetimes of various Er-doped sputtered samples after an anneal at 1000°C for 1 hour. Courtesy of Dr. Sajan Saini.

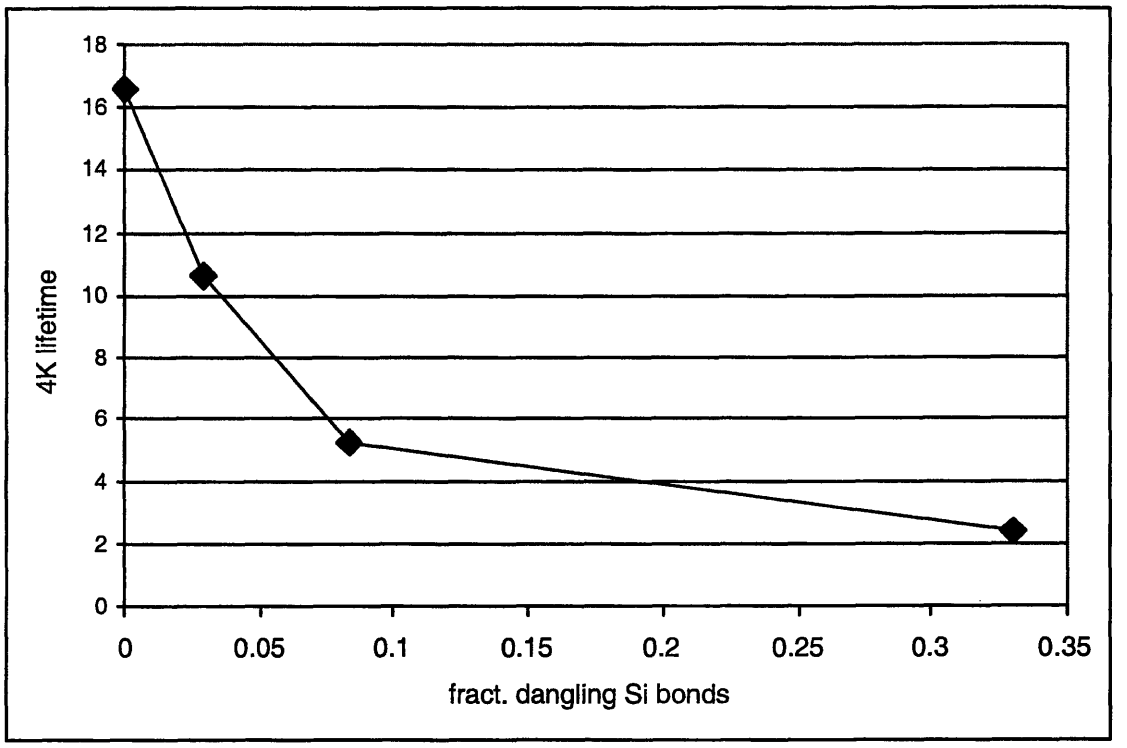

Figure 6.1: 4K lifetimes vs. number of Si dangling bonds.

Much as we were able to correlate waveguide loss to the number of dangling silicon bonds, the PL lifetimes of the Er-doped samples also correlate to dangling Si bonds. Figure 6.1 shows how the 4K lifetimes vary with the fraction of dangling Si bonds. (Please see Chapter 5 for the determination of dangling bond number based on refractive index and processing conditions.)

Figure 6.1 demonstrates that the best lifetimes are observed in materials with the lowest number of dangling Si bonds.

6.1.4 Conclusions

Sputtered silicon oxynitride, nitride, and oxide are shown to be viable hosts for erbium atoms. Photoluminescence in the 1550 nm wavelength window is demonstrated. The lifetimes of this luminescence is shown to approach that of a commercial CVD process in the case of sputtered SiO_2 and cosputtered SiON. These materials are ideal candidates for investigating potential gain in erbium-doped waveguides.

Chapter 7

Conclusions and Future Work

7.1 Research Summary

The previous chapters have illustrated a variety of developments in silicon oxynitride processing for microphotonics applications. A materials study of sputtered silicon oxynitride and sputtered silicon nitride is presented. Sputtered silicon oxynitride is shown to be a well-controlled material which possesses many of the characteristics required of a good optical material, including easy refractive index control, low to moderate film stresses, homogeneous film composition, and low film roughness. Residual gas analysis is performed on a variety of reactive and co-sputter processes from dielectric targets. Models are presented to explain the properties of co-sputtered SiON and to describe the oxidation behavior of reactively sputtered SiON. Cosputtered SiON deposition is shown to be controlled by a mixture model, while reactive SiON deposition is shown to be either a Si-flux limited or a O-flux limited process (depending on oxygen partial pressure and target power). Slab

SiON waveguides are produced using both room temperature reactive and co-sputtered deposition processes, and as-deposited waveguide losses below 0.7 dB/cm are shown to be achievable. Si-dangling bonds are shown to contribute to the materials loss in SiON waveguides. Finally, cosputtered SiON and sputtered SiO_2 are shown to have lifetimes on the order of commercial EDFA material, and non-radiative energy transfer in Er-doped SiON is shown to correlate with Si-dangling bonds.

This work has shown sputter processed silicon oxynitride to be a very promising material for microphotonics, and this research has provided a deeper understanding of sputter processing for optical applications. There are a number of applications in which the potentials of sputtered SiON could be fully exploited. These applications are outlined below.

7.2 A Variety of Waveguide-Based Devices

This thesis has demonstrated that low-loss slab waveguides can be produced using sputter deposition. A wide range of waveguide core indices have been demonstrated, exploiting one of the most appealing things about the SiON materials system – its flexibility. In particular, losses below 1.0 dB/cm have been shown for as-deposited SiON films with indices greater than 1.65, a particularly difficult index range to achieve using traditional SiON processing methods.

The utility of these low-loss materials is not limited to the slab waveguides shown, or even to the channel waveguides demonstrated in Si_3N_4. These waveguides can be employed for

any application for which low-loss and index flexibility are required. Such applications include channel and ridge waveguides, ring resonators, arrayed waveguide gratings, fiber-to-waveguide couplers, and power splitters. Introducing sputter processing to these devices would allow for a greater flexibility in index choice, and therefore a greater flexibility in device design could be achieved.

7.3 Integrated Optoelectronics

The utility of the sputter process method becomes particularly clear when we begin to consider the integration of a variety of microphotonic devices. Most of the microphotonics research to date has focused on the development and optimization of individual components for optical performance. The production of lasers, detectors, waveguides, modulators, and amplifiers has been studied, but the integration of these components has not been fully considered. For this reason, much waveguide research has focused on processing techniques that would make the integration of these waveguides with other devices either very difficult or impossible. For example, low-index PECVD SiON waveguides have been realized with losses below 1 dB/cm. However, such device performance can require anneals of many hours at temperatures approaching 1200°C. Furthermore, waveguide losses absent of these high temperature anneals approach 10 dB/cm for lower-index contrast SiON waveguides.

These high-temperature processing steps can be contrasted with the requirements for good detector performance. Semiconductor diodes require precise levels of dopants to be placed in precise locations. Deviations from these precise conditions lead to a degradation in device

performance. High temperature anneals promote diffusion which radically changes dopant profiles. The high-temperature annealing steps required to produce high-quality PECVD silicon oxynitride simply cannot be applied to detector diodes. Traditional PECVD waveguide processing places severely limits the potential for fully integrated silicon microphotonics.

Alternatively, the waveguide sputter processes presented in this work are all low thermal budget processes. All deposition is performed at room temperature, and SiON slab waveguide losses below 0.7 dB/cm have been achieved without any annealing treatment whatsoever. This low thermal budget processing will give a great advantage when integrating waveguides with temperature-sensitive devices such as detector diodes.

7.4 Erbium-doped Materials

Sputter processing provides an easy method for doping films. Unlike CVD processing, which required an appropriate carrier gas for all dopants, sputter processing simply requires that a solid target be available. This flexibility in doping becomes particularly important when designing specialty materials for microphotonics, such as erbium-doped materials for light amplification.

7.5 Final Remarks

In this work, sputtered silicon oxynitride has been shown to be a material capable of providing low optical losses while maintaining flexibility in index and processing conditions. The materials properties of the SiON system have been studied, and models have been established to determine the ideal processing conditions for low-loss waveguide deposition. Photoluminescence of Er-doped SiON with long lifetimes is demonstrated. Further research has been outlined to fully establish sputtered silicon oxynitride as a material ideal for use in a variety of waveguiding devices, in integrated microphotonic systems, and in light amplifiers.

Bibliography

[1] A. Glass, D. DiGiovanni, T. Strasser, A. Stentz, R. Slusher, A. White, A. R. Kortan, and B. Eggleton, Bell Labs Technical Journal, pp. 168-87, 2000.

[2] *International Technology Roadmap for Semiconductors, 2003 Executive Summary*, Semiconductor Industry Association, 2003.

[3] E.A. Fitzgerald, and L.C. Kimerling, *MRS Bulletin*, **23**(4), pp. 39-47.

[4] W. Dautremont-Smith, R.J. McCoy, R. H. Burton and A. G. Baca, *AT&T Technical Journal*, Jan./Feb. 1989, pp. 64-82.

[5] B.E.A. Saleh, and M.C. Teich, *Fundamentals of Photonics*, John Wiley & Sons, Inc, New York, 1991.

[6] J. Foresi, *Optical Confinement and Light Guiding in High Dielectric Contrast Materials Systems*. PhD Thesis, MIT, 1997.

[7] T. Miyashita, *Electronic Components and Technology Conference, 1990, Proceedings, 40th*,vol. 1, 20-23 May 1990, pp. 55-59.

[8] Y. Li, C. H. Henry, *Optoelectronics, IEE Proceedings*, vol. 143, no. 5, 1996, pp. 263-280.

[9] D. R. Lim, *Device Integration for Silicon Microphotonic Platforms*, PhD Thesis, MIT, 2000.

[10] T. Miya, *IEEE Journal of Selelcted Topics in Quantum Electronics*, Vol. 6, No. 1, 2000, pp. 38-45.

[11] W.D. Westwood, *Sputter Deposition*, New York(AVS):2003.

[12] M. Ohring, *The Materials Science of Thin Films*, Boston(Academic Press):1992.

[13] S. Campbell, *The Science and Engineering of Microelectronic Fabrication*, New York(Oxford University Press):1996.

[14] R. Ulrich, R. Torge, *Applied Optics*, **12**(12), pp. 2091-8.

[15] G.L. Bona, R. Germann, F. Horst, B.J. Offrein, and H.W.M. Salemink, *Parallel Interconnects 1999 Proceedings. The 6th International Conference* 17-19 Oct. 1999, pp. 145-148.

[16] K. Worhoff, R. de Ridder, P. Lambeck, and A. Driessen, *Lasers and Electo-Optics Society Annual Meeting 1998 IEEE*, vol. 2, 1-4 Dec. 1998, vol. 2, pp. 370-371.

[17] R.M. de Ridder, K. Worhoff, A. Driessen, P.V. Lambeck, and H. Albers, *IEEE Journal of Selected Topics in Quantum Electronics*, vol. 4, pp. 930-937, 1998.

[18] R. Germann, H.W.M. Salemink, R. Beyeler, G.L. Bona, F. Horst, I. Massarek, and B.J. Offrein, *Journal of the Electrochemical Society*, vol. 147, pp. 2237-41, 2000.

[19] Metricon Model 2010 Prism Coupler Manual, Metricon Corp.

[20] K.K. Lee, D.R. Lim, A. Agarwal, D. Ripin, H. Fujimoto, M. Morse, and L.C. Kimerling, *Optical Devices for Fiber Communication*, Proceedings of the SPIE, vol. 3847, pp. 120-5, 1999.

[21] K. Worhoff, A. Driessen, P.V. Lambeck, L.T.H. Hilderink, P.W.C. Linders, T.J.A. Popma, *Sensors and Actuators*, vol. 74, pp. 9-12, 1999.

[22] H.W.M. Salemink, P.Horst, R. Germann, B.J. Offrein, and G.L. Bona, *Materials Research Society Proceedings*, vol. 574, pp. 225-260, 1999.

[23] F. Ay, A. Aydinh, C. Roeloffzen, A. Dresden, *Lasers and Electro-Optics Society 2000 Annual Meeting, 13 Annual Meeting, IEEE*, vol. 2, 13-16 Nov. 2000, pp. 760-761.

[24] S.P. Speakman, P.M. Read, and A. Kiermasz, *Vacuum*, vol. 38, pp. 183-188, 1988.

[25] H. Albers, L.T.H. Hilderink, E. Szilagyi, F. Paszti, P.V. Lambeck, and Th.J.A. Popma, *Lasers and Electro-Optics Society Annual Meeting, 1995, 8th Annual Meeting, IEEE*, vol. 2, 30-31 Oct. 1995, pp. 88-89.

[26] O. Sanchez, J.M. Martinez-Duart, R.J. Gomez-Sanroman, R. Perez-Casero, M.A. Aguilar, C. Falcony, F. Fernandez-Gutierrez, M. Hernandez-Velez, SiO_xN_y Films Deposited with $SiCl_4$ by Remote Plasma Enhanced CVD, *Journal of Materials Science*, vol. 34, pp. 3007-3012, 1999.

[27] K. Worhoff, P.V. Lambeck, and A. Driessen, Design, Tolerance Analysis, and Fabrication of Silicon Oxynitride Based Planar Optical Waveguides for Communication Devices, *Journal of Lightwave Technology*, vol. 17, pp. 1401-1407, 1999.

[28] C.M.M. Denisse, K.Z. Troost, F.H.P.M. Habraken, W.F. van der Weg, and M. Hendriks, Annealing of Plasma Silicon Oxynitride Films, *Journal of Applied Physics*, vol. 60, pp. 2543-2547, 1986.

[29] S.V. Hattangady, H. Niimi, and G. Lucovsky, Integrated Processing of Silicon Oxynitride Films by Combined Plasma and Rapid-Thermal Processing, *Journal of Vacuum Science and Technology*, vol. 14, pp. 3017-3023, 1996.

[30] A. del Prado, I. Martil, M. Fernandez, G. Gonzalez-Diaz, Full Composition Range Oxynitride Films Deposited by ECR-PECVD at Room Temperature, *Thin Solid Films*, vol. 343-344, pp. 437-440, 1999.

[31] D. Schalch, A. Scharmann, and R. Wolfrat, The Role of Hydrogen in Silicon Nitride and Silicon Oxynitride Films, *Thin Solid Films*, vol 124, pp. 301-308, 1985.

[32] M. Serenyi, M. Racz, and T. Lohner, Refractive Index of Sputtered Silicon Oxynitride Layers for Antireflection Coating, *Vacuum*, vol. 61, pp. 245-249, 2001.

[33] T.S. Eriksson, and C.G. Granqvist, Infrared Optical Properties of Silicon Oxynitride Films: Experimental Data and Theoretical Interpretation, *Journal of Applied Physics*, vol. 60, pp. 2081-2091, 1986.

[34] D. Gao, Y. Kashiwazaki, K. Muraoka, H. Nakashima, K. Furukawa, Y. Liu, and T. Tsurushima, Deposition of High-Quality Silicon Oxynitride Film at Low Temperature by Using a Sputtering-Type Electron Cyclotron Resonance Plasma, *Japanese Journal of Applied Physics*, vol. 36, pp. L1692-L1694, 1997.

[35] H. Reinhardt, D. Schalch and A. Scharmann, Determination of the Composition of Sputtered Silicon Oxynitride Films by Auger Electron Spectroscopy and Rutherford Backscattering Spectrometry, *Thin Solid Films*, vol. 167, pp. L1-L5, 1988

[36] H. Takahashi, A. Nishiguchi, H. Nagata, H. Kataoka, M. Fujishima, Structural Relaxation and Stress Reduction in Hydrogenated Silicon Oxide Films, *Journal of Applied Physics*, vol. 79, pp. 2782-2789, 1996.

[37] R. Germann, R. Beyeler, G.L. Bona. F. Horst, B.J. Offrein, and H.W.M. Salemink, *Optical Fiber Communication Conference 1999 and the International Conference on Integrated Optics and Optical Fiber Communications, Technical Digest*, vol. 2, 21026 Feb. 1999, pp. 268-270.

[38] B.J. Offrein, G.L. Bona, R. Germann, F. Horst, H.W.M. Salemink, *Lasers and Electro-Optics Society 1999, 12 Annual Meeting, IEEE*, vol. 2, 8-11 Nov. 1999, pp. 547-548.

[39] B.J. Offrein, R. Germann. G.L. Bona, F. Horst, and H.W.M. Salemink, Tunable Optical Add/Drop Components in Silicon-Oxynitride Waveguide Structures, *ECOC*, pp. 325-326, 1998.

[40] B.J. Offrein, F. Horst, G.L. Bona, R. Germann, H.W.M. Salemink, and R. Beyeler, Adaptive Gain Equalizer in High-Index-Contrast SiON Technology, *IEEE Photonics Technology Letters*, vol. 12, pp. 504-506, 2000.

[41] B.J. Offrein, F. Horst. G.L. Bona, H.W.M. Salemink, R. Germann, and R. Beyeler, Wavelength Tunable 1-from-16 and Flat Passband 1-From-8 Add-Drop Filters, *IEEE Photonics Technology Letters*, vol. 11, pp. 1440-1442, 1999.

[42] B.J. Offrein, F. Horst, G.L. Bona, R. Germann, and H.W.M. Salemink, Tunable WDM Add/Drop Components in Silcon-Oxynitride Waveguide Technology, *Electronic Components and Technology Conference*, pp. 19-25, 1999.

[43] B.J. Offrein, R. Germann, F. Horst. H.W.M. Salemink. R. Beyeler, and G.L. Bona, Resonant Coupler-Based Tunable Add-After-Drop Filter in Silicon-Oxynitride Technology for WDM Networks, *IEEE Journal of Selected Topics in Quantum Electronics*, vol. 5, pp. 1400-1406, 1999.

[44] C.G.H. Roeloffzen, F.Horst, B.J. Offrein, R. Germann. G.L. Bona. H.W.M. Salemink, and R. M. de Ridder, Tunable Passband Flattened 1-from-16 Binary-Tree Structured Add-After-Drop Multiplexer Using SiON Waveguide Technology, *IEEE Photonics Technology Letters*, vol. 12, pp. 1201-1203, 2000.

[45] S. Rotolo, A. Tanzi, S. Brunazzi, D. DiMola, L. Cibinetto, M. Lenzi, G.L. Bona, B.Jl. Offrein, F. Horst, R. Germann. H.W.M. Salemink, and P.H. Baechtold, Integrated Optic Tunable Add-Drop Filters for WDM Ring Networks, *Journal of Lightwave Technology*, vol. 18, pp. 569-578, 2000.

[46] M. Hoffmann, P. Kopka, and E. Voges, Low-Loss Fiber-Matched Low-Temperature PECVD Waveguides with Small-Core Dimensions for Optical Communications Systems, *IEEE Photonics Technology Letters*, vol. 9, pp. 1238-1240, 1997.

[47] M.J. Hernandez, J. Garrido, J. Martinez, and J. Piqueras, Compositional and Electrical Properties of ECR-CVD Silicon Oxynitrides, *Semiconductor Science and Technology*, vol. 12, pp. 927-932, 1997.

[48] F. Horst, E. Fluck, B.J. Offrein, R. Germann, H.W.M. Salemink, and G.L. Bona, Compace 1-to-8, Double 1-to-4 or Fourfold 1-to-2 Space Switch Based on Beam Steering by a Waveguide Array, *Electronic Components and Technology Conference*, pp. 922-926, 1999.

[49] M. Hoffmann, P. Kopka, and E. Vorges, Thermooptical Digital Switch Arrays in Silica-on-Silicon with Defined Zero-Voltage State, *Journal of Lightwave Technology*, vol. 16, pp. 395-400, 1998.

[50] M. Spuhler, B. Offrein, G.L. Bona, R. Germann. I. Massarek, D. Erni, A Very Short Planar Silica Spot-Size Converter Using a Nonperiodic Segmented Waveguide, *Journal of Lightwave Technology*, vol. 16, pp. 1680-1685, 1998.

[51] A. V. Chelnokov, J.M. Lourtioz, P. Boucaud, H. Bernas, J. Chaumont, and T. Plowman, Deep High-Dose Erbium Implantation of Low-Loss Silicon Oxynitride Waveguides, *Electronics Letters*, vol. 30, pp. 1850-1852, 1994.

[52] K. Worhoff, B.J. Offrein, A. Driessen, P.V. Lambeck, G.L. Bona, and T.J. A. Popma, Birefringence Compensation in Double-Core Optical Waveguides, *ECOC*, pp.605-606, 20-24 September, 1998.

[53] K. Worhoff, B.J. Offrein, P.V. Lambeck, G.L. Bona, and A. Driessen, Birefringence Compensation Applying Double-Core Waveguiding Structures, *IEEE Photonics Technology Letters*, vol. 11, pp. 206-208, 1999.

[54] G. Lucovsky, P.D. Richard, D.V. Tsu, S.Y. Lin, and R. J. Markunas, *J. Vac. Sci. Technol. A* 4 (3) 1986, pp. 681-8.

[55] D.V. Tsu, G. Lucovsky, and M.J. Mantini, *Physical Review B*, V. 33 n.10 1986, pp. 7069-76.

[56] B.S. Sahu, O.P. Agnihotri, S.C. Jain, R. Mertens, and I. Kato, *Semicond. Sci. Technol.* **15**(1000) L11-L14.

[57] J. Viard, E. Beche, D. Perarnau, B. Berjoan, and J. Durand, *Journal of the European Ceramic Society* **17** (1997) 2025-2028.

[58] D. Criado, I. Pereyra, M.I. Alayo, *Materials Charactarization*, 50 (2003), 167-171.

[59] A. del Prado, I. Martil, M. Fernandez, G. Gonzalez-Diaz, *Thin Solid Films*, 343-344 (1999) 437-440.

[60] D.V. Tsu, G. Lucovsky, M.J. Mantini, and S.S. Chao, *J. Vac. Sci. Technol. A* 5 (4) 1987, pp 1998-2002.

[61] M. Vila, C. Prieto, J. Garcia-Lopez, M. A. Respaldiza, *Nuclear Instruments & Methods in Physics Research B* v. 211, n 2, 2003, p 199-205.

[62] M. Vila, J.A. Martin-Gago, A. Munoz-Martin, C. Prieto, P. Miranzo, M.I. Osendi, J. Garcia-Lopez, M. A. Respaldiza, Vacuum 67(2002) 513-518.

[63] G.-L. Bona, R. Germann, B.J. Offrein, IBM J. Res. & Dev. Vol. 47, n 2/3, 2003, p 239-249.

[64] J. Lee, K. Cheng, J. Lyding, and H.W.M. Salemink, *Materials Research Socitey Symposium Proceedings* vol. 609, 2000, pp. A26.8.1.

[65] A. Shih, S.-H. Yeh, S.-C. Lee, T. Yang, *Journal of Applied Physics*, vol. 89, no. 10, 2001, pp. 5355-5361.

[66] Y. Wang, R. Yue, H. Han, and X Liao, *Journal of Non-Crystalline Solids* 291, (2001), pp. 107-112.

[67] V.A. Volodin, M.D. Efremov, V.A. Gritsenko, and S.A. Kochebei, *Applied Physics Letters*, Vol. 73, No. 9, (1998), pp. 1212-1214.

[68] C. Cook, T. Daly, R. Liu, M. Canonico, Q. Xie, R.B. Gregory, S. Zollner, *Thin Solid Films*, 455-456, (2004), pp. 794-797.

[69] J. Bandet, B. Despax, M. Caumont, *Journal of Applied Physics*, vol. 85, no. 11, 1999, pp. 7899-7904.

[70] K.-C. Lin, S.-C. Lee, *Journal of Applied Physics* **72**(11), 1992, pp. 5474-5482.

[71] S. Huet, G. Viera, L. Boufendi, *Thin Solid Films*, 403-404, (2002), pp. 193-196.

[72] H. Xia, Y. L. He, L. C. Wang. W. Zhang. X.N. Liu, X.K. Zhang, D. Feng, H. Jackson, *Journal of Applied Physics*, **78** (11), 1995, pp. 6705-6708.

[73] Z. Iqbal, S. Veprek, A.P. Webb, P. Capezzuto, *Solid State Communications*, Vol. 37, pp.993-996.

[74] M. I. Nathan, J. E. Smith Jr., K.N. Tu, *Journal of Applied Physics*, vol. 45, no. 5, 1954. p. 2370.

[75] H.-S. Han, S.-Y. Seo, J. H. Shin, and N. Park, *Applied Physics Letters*, vol. 81, no. 20, (2002), pp. 3720-22.

[76] H.-S. Han, S.-Y. Seo, and J.H. Shin, *Applied Physics Letters* vol. 79, no. 27, (2001), pp. 4568-70.

[77] K. Luterova, I. Pelant, I. Mikulskas, R. Tomasiunas, D. Muller, J.-J. Grob, J.-L. Rehspringer, and B. Honerlage, *Journal of Applied Physics*, vol. 91, no. 5. (2001), pp. 2896-2900.

[78] W. L. Wilson, P.F. Szajowski, L.E. Brus, *Science*, vol. 262, (1993), pp. 1242-44.

[79] D. Pacifici, G. Franzo, F. Priolo, F. Iacona, and L. Dal Negro, *Physical Review B*, **67**, (2003), pp. 245301-1 to 12.

[80] L. Dal Negro, M. Cazzanelli, L. Pavesi, S. Ossicini, D. Pacifici, G. Franzo, F. Priolo, and F. Iacona, *Applied Physics Letters*, vol. 82, no. 26, (2003), pp. 4636-38.

[81] L. Pavesi, L. Dal Negro, C. Mazzoleni, G. Franzo, and F. Priolo, *Nature*, vol. 408, (2000), pp. 440-44.

[82] L.T. Canham, *Applied Physics Letters*, vol. 57, no. 10, (1990), pp. 1046-8.

[83] O. Bisi, S. Ossicini, and L. Pavesi, *Surface Science Reports*, no. 38, (2000), pp. 1-126.

[84] D. J. DiMaria, J.R. Kirtley, E.J. Pakulis, D.W. Dong, T.S. Kuan, F.L. Pesavento, T. N. Theis, J. A. Cutro, and S.D. Brorson, *Journal of Applied Physics*, vol. 56, no. 2, (1984), pp. 401-16.

[85] J. P. Proot, C. Delerue, and G. Allan, *Applied Physics Letters*, vol. 61, no. 16, (1992), pp. 1948-50.

[86] M.V. Wolkin, J. Jorne, P.M. Fauchet, G. Allan, and C. Delerue, *Physical Review Letters*, vol. 82, no. 1, (1999), pp. 197-200.

[87] P. Ball, *Nature*, vol. 409, (2001), pp. 974-976.

[88] S. Saini, J. Sandland, A. Eshed, D.K. Sparacin, L. DalNegro, J. Michel, and L.C. Kimerling, AAA High Index Contrast Silicon Oxynitride Materials Platform for Er-doped Microphotonic Amplifiers,, to be published in MRS Proceedings, Spring 2004.

[89] L.C. Kimerling, L. Dal Negro, S. Saini, Y.Yi, D. Ahn, S. Akiyama, D. Cannon, J. Liu, J. Sandland, D. Sparacin, and M. Watts, MMMonolithic Silicon Mircophotonics,, in *Silicon Photonics, Topics in Applied Physics, no. 94*, L. Pavesi, D.J. Lockwood, eds., Springer-Verlag, New York, 2004, pp. 89-117.

[90] F. Giorgis, C. F. Pirri, C. Vinegoni, and L. Pavesi, *Physical Review B* vol. 60, no. 16, (1999), pp 572-6.

[91] F. Giorgis, C. Vinegoni, and L. Pavesi, *Physical Review B* vol. 61, no. 7, (2000), pp. 4693-8.

[92] F. Giorgis, *Applied Physics Letters*, vol. 77, no.4, (2000), pp. 522-4.

[93] F. Giorgis, P. Mandracci, L. Dal Negro, C. Mazzoleni, and L. Pavesi, *Journal of Non-Crystalline Solids*, 266-269, (2000), pp. 588-92.

[94] H. Kato, N. Kashio, Y. Ohki, K.S. Seol, T. Noma, *Journal of Applied Physics*, vol. 93, no. 1, (2003), pp. 239-41.

[95] D.J. Dunstan, F. Boulitrop, *Physical Review B*, vol. 30, no. 10, (1984), pp. 5945-51.

[96] F. Boulitrop, D.J. Dunstan, *Physical Review B*, vol. 28, no. 10, (1983), pp. 5923-29.

[97] Bansal, N., *Handbook of Glass Properties*, Academic Press, Orlando, 1986.

[98] S.K. Ray, S. Das, C.K. Maiti, S.K. Lahiri, and N.B. Chakraborti, *Journal of Applied Physics*, vol. 75, no. 12, (1994), pp. 8145-52.

[99] W.-T. Li, D.R. McKenzie, W.D. McFall, and Q.-C. Zhang, *Thin Solid Films*, vol. 384, (2001), pp. 46-52.

[100] K. Worhoff, L.T.H. Hilderink, A. Driessen, and P.V. Lambeck, *Journal of the Electrochemical Society*, vol. 149, no. 8, (2002), pp. F85-F91.

[101] B. Schauwecker, M. Arnold, C.V. Radehaus, G. Przyrembel, and B. Kuhlow, *Opt. Eng.*, vol. 41, no. 1, (2002), pp. 237-43.

[102] G. Xu, P. Jin, M. Tazawa, and K. Yoshimura, *Thin Solid Films*, vol. 425, (2003), pp. 196-202.

[103] S.K. Patra, and G. Mohan Rao, *Materials Science and Engineering*, vol. B90, (2002), pp. 90-8.

[104] A. Himeno, K. Kato, *IEEE Journal of Selected Topics in Quantum Electronics*, vol. 4, no. 6, (1998), pp. 913-924.

[105] R. Schubert, *Partial Pressure Analyzers, Analysis, and Applications*, American Vacuum Society, New York, 2000.

[106] J.S. Coursey, D.J. Schwab, and R.A. Dragoset, *Atomic Weights and Isotopic Compositions*, NIST Physics Library, www.physics.nist.gov/PhysRefData/Compositions/index.html, 2003.

[107] Conversations with John Jackson, Metricon Corporation

[108] S. Saini, J.G. Sandland, A. Eshed, D.K. Sparacin, L. Dal Negro, "High Index Contrast Silicon Oxyniride Materials Platform for Er-Doped Microphotonics", to be published in MRS Proceedings, Spring 2004.

[109] S. Berg, H-O. Blom, T. Larsson, and C. Nender, *J. Vac. Sci. Technol. A* **5**(2), Mar/Apr 1987, pp. 202-7.

[110] S. Berg, H.-O. Blom, M. Moradi, C. Nender, and T. Larsson, *J. Vac. Sci. Technol. A* **7**(3), May/June 1989, pp. 1225- 1229.

[111] S. Berg, T. Larsson, C. Nender, and H.-O. Blom, *J. Appl. Phys.* **63**(3), 1988, pp. 887-891.

[112] P. Carlsson, C. Nender, H. Barankova, and S. Berg, *J. Bac. Sci. Technol. A* **11**(4) 1993, pp. 1534-1539.

[113] *J. Vac. Sci. Technol. A* **6**(3), 1988, pp. 1832-1836.

[114] F. C. Stedile, I. J. R. Baumvol, W.H. Schreiner, F.L. Freire Jr. *J. Vac. Sci. Technol. A* **10**(3) 1992, pp. 462- 467.

[115] L. Pinard and J.M. Mackowski, *Applied Optics*, vol. 36, no. 22, 1997, pp. 5451-5460.

[116] G.-L. Bona, R. Germann, B.J. Offrein, *IBM J. Res & Dev.* vol. 47, no. 2/3, March/May 2003.

[117] S. Saini, *Gain Efficient Waveguide Optical Amplifiers for Si Microphotonics*, Ph.D. Thesis, MIT, 2004.